

1    **Accurate Elucidation of Oxidation Under Heavy Ozone**  
2    **Pollution: A Full Suite of Radical Measurement In the**  
3    **Chemical-complex Atmosphere**

4    Renzhi Hu<sup>1</sup>, Guoxian Zhang<sup>1,2,×</sup>, Haotian Cai<sup>1</sup>, Jingyi Guo<sup>1</sup>, Keding Lu<sup>4</sup>, Xin Li<sup>4</sup>,  
5    Shengrong Lou<sup>5</sup>, Zhaofeng Tan<sup>4</sup>, Changjin Hu<sup>1</sup>, Pinhua Xie<sup>1,3, \*\*</sup>, Wenqing Liu<sup>1,3</sup>

6    <sup>1</sup> Key Laboratory of Environment Optics and Technology, Anhui Institute of Optics and Fine  
7    Mechanics, HFIPS, Chinese Academy of Sciences, Hefei, China

8    <sup>2</sup> School of Physics and New Energy, Xuzhou University of Technology, Xuzhou, China

9    <sup>3</sup> College of Resources and Environment, University of Chinese Academy of Science, Beijing, China

10    <sup>4</sup> State Key Joint Laboratory of Environmental Simulation and Pollution Control, College of  
11    Environmental Sciences and Engineering, Peking University, Beijing, China

12    <sup>5</sup> State Environmental Protection Key Laboratory of the Formation and Prevention of Urban Air  
13    Pollution Complex, Shanghai Academy of Environmental Sciences, Shanghai, China

14    **Correspondence to:** Guoxian Zhang, School of Physics and New Energy, Xuzhou  
15    University of Technology, Xuzhou, China

16    **Correspondence to:** Pinhua Xie, Key Laboratory of Environment Optics and  
17    Technology, Anhui Institute of Optics and Fine Mechanics, HFIPS, Chinese Academy of  
18    Sciences, Hefei, China

19    **Email addresses:** gxzhang@aiofm.ac.cn (Guoxian Zhang); phxie@aiofm.ac.cn (Pinhua  
20    Xie)

21  
22

23 **Abstract:** The Yangze River Delta (YRD) in China encountered with prolonged ozone  
24 pollution in September 2020, which had significant impacts on the respiratory,  
25 dermatological, and visual health of local residents. To accurately elucidate the  
26 limitations of oxidation processes in the chemical-complex atmosphere, a full suite of  
27 radical measurements (OH, HO<sub>2</sub>, RO<sub>2</sub>, and  $k_{OH}$ ) was established in YRD region for the  
28 first time. The diurnal peaks of radicals exhibited considerable variation due to  
29 environmental factors, showing ranges of  $3.6$  to  $27.1 \times 10^6$  cm<sup>-3</sup> for OH,  $2.1$  to  $33.2 \times 10^8$   
30 cm<sup>-3</sup> for HO<sub>2</sub>, and  $4.9$  to  $30.5 \times 10^8$  cm<sup>-3</sup> for RO<sub>2</sub>. At a heavy ozone pollution episode, the  
31 oxidation capacity reached an intensive level compared with other sites, and the  
32 simulated OH, HO<sub>2</sub>, and RO<sub>2</sub> radicals provided by the RACM2-LIM1 mechanism failed  
33 to adequately match the observed data both in radical concentration and experimental  
34 budget analysis. Sensitivity tests utilizing a comprehensive set of radical measurements  
35 revealed that the higher aldehyde mechanism (HAM) effectively complements the  
36 non-traditional regeneration of OH radicals, yielding enhancements of 4.4% - 6.0%  
37 compared to the base scenario, while the concentrations of HO<sub>2</sub> and RO<sub>2</sub> radicals have  
38 shown increments of about 7.4% and 12.5%, respectively. Notably, RO<sub>2</sub> radical  
39 concentrations exhibit a pronounced sensitivity to autoxidation, with the incorporation of  
40 additional OVOCs potentially boosting simulated RO<sub>2</sub> radical concentrations by 20% to  
41 40%. The incorporation of larger alkoxy radicals stemming from monoterpenes has  
42 refined the consistency between measurements and modeling in the context of ozone  
43 production under elevated NO levels, diminishing the disparity from 4.17 to 2.33. This  
44 outcome corroborates the hypothesis of sensitivity analysis as it pertains to ozone  
45 formation. Moving forward, by implementing a comprehensive radical detection  
46 approach, further investigations should concentrate on a broader range of OVOCs to  
47 rectify the imbalance associated with RO<sub>2</sub> radicals, thereby providing a more precise  
48 understanding of oxidation processes during severe ozone pollution episodes.

49

50 **Keywords:** FAGE-LIF; Full-chain detection; Radical; P(Ox); OVOCs;

51

## 52 1 Introduction

53 In recent years, China's rapid economic development has led to severe environmental  
54 pollution problems, which significantly impacted the respiratory, dermatological, and visual  
55 health of local residents (Wang et al., 2022c; Huang et al., 2018). This has raised  
56 concerns about the coexistence of regional primary and secondary pollution, making air  
57 quality improvement efforts a focal point (Liu et al., 2021; Wang et al., 2022a). In the  
58 complex atmosphere, near-surface ozone ( $O_3$ ) is formed through continuous  
59 photochemical reactions between nitrogen oxides ( $NO_x \equiv NO + NO_2$ ) and volatile  
60 organic compounds (VOCs) under light conditions, while hydroxyl radicals ( $OH$ ) serve  
61 as the main oxidant in the troposphere, converting VOCs into hydroperoxy ( $HO_2$ ) and  
62 organic peroxy ( $RO_2$ ) radicals (Rohrer et al., 2014; Hofzumahaus et al., 2009).  
63 Additionally, the oxidation of nitric oxide (NO) and peroxy radicals produce nitrogen  
64 dioxide ( $NO_2$ ), which is the sole photochemical source of ozone (Lu et al., 2012; Stone et  
65 al., 2012).

66 Despite numerous experimental and theoretical explorations to establish the  
67 radical-cored photooxidation mechanism in the troposphere, field observations were  
68 primarily focused on  $HO_x$  ( $HO_x \equiv OH + HO_2$ ) radicals due to the limitations of detection  
69 technology (Kanaya et al., 2012; Lu et al., 2012; Hofzumahaus et al., 2009; Yugo Kanaya  
70 and Tanimoto, 2007; Ren et al., 2008; Stone et al., 2012; Levy, 1971). Recent  
71 advancements in detection technology, such as the application of a new LIF technique  
72 ( $RO_x$ LIF), have made the detection of  $RO_2$  radicals possible (Whalley et al., 2013; Tan et  
73 al., 2017a). Moreover, the union of comprehensive field campaigns and box model, has  
74 proven to be an effective method for verifying the integrity of radical chemistry at local  
75 to global scales (Lu et al., 2019b; Tan et al., 2018). Several experiments have indicated  
76 that the existing atmospheric chemical mechanism posted challenges in deepening the  
77 understanding of the regional pollution explosion (Whalley et al., 2021; Slater et al., 2020;  
78 Tan et al., 2017a; Woodward-Massey et al., 2023). For instance, the observation of up to  
79  $4 \times 10^9 \text{ cm}^{-3}$  of  $RO_2$  radical in the center of Beijing in 2017 (APHH) was significantly  
80 underestimated by the MCM v3.3.1 mechanism (Whalley et al., 2021). Further exploring  
81 the unrepeatable concentration and the oxidation process in the chemical-complex  
82 atmosphere is deemed necessary (Whalley et al., 2021; Woodward-Massey et al., 2023).

83 The YRD region, situated between the North China Plain (NCP) and Pearl River  
84 Delta (PRD), is highly prone to regional transport interactions and aerosol-boundary layer  
85 feedback (Jia et al., 2021; Huang et al., 2020). In September 2020, the YRD region  
86 experienced a severe episode of secondary pollution, with both the daily maximum  
87 8-hour average ozone (MDA8) and daily average  $PM_{2.5}$  concentrations surpassing the  
88 pollution threshold, distinguishing it from other megacities (Fig. S1). In an effort to gain  
89 a better understanding between the complex radical chemistry and the intensive oxidation  
90 level, TROPSTECT-YRD (The experiment on Radical chemistry and Ozone Pollution  
91 perSpectively: long-Term Elucidation of the photochemiCal oxidaTion in the Yangze  
92 River Delta) was conducted in Hefei during September 2020. Accurate elucidation of the  
93 oxidation process under heavy ozone pollution was provided by a full suite of radical  
94 measurement ( $OH$ ,  $HO_2$ ,  $RO_2$  and  $k_{OH}$ ) in the chemical-complex atmosphere.

## 95 **2 Materials and methods**

### 96 **2.1 Site description and instrumentation**

97 The TROPSTECT observation was conducted from 1 to 20 September 2020 at the  
98 Science Island background station ( $31.9^{\circ}$  N,  $117.2^{\circ}$ E) in Hefei, a typical megacity located  
99 in the central region of Anhui Province within the Yangtze River Delta. The station is  
100 situated on a peninsula with abundant vegetation to the northwest of urban areas and is in  
101 close proximity to Dongpu Lake, which is only 200 meters away, and the main road,  
102 positioned 250 meters southward (Fig. 1). Consequently, the relatively enclosed  
103 environment exhibits typical suburban characteristics of anthropogenic emissions. The  
104 station is located in the transition region between urban and suburban areas, reflecting the  
105 regional transpor of pollution in Hefei and its surrounding areas.



106 **Fig. 1. (a)** The location of the measurement site (source: © Google Earth).  
107 **(b)** The close shot of the measurement site location (source: © Google Earth).  
108 **(c)** The actual image for the LIF-Box.  
109

110       Regarding the instrumentation, a group of oxidation-related instruments were  
111       installed on the 7th floor of the Comprehensive Building at the Anhui Institute of Optics  
112       and Fine Mechanics (AIOFM), with all sampling outlets positioned more than 20 meters  
113       above the ground. The details of the instruments measuring various parameters such as  
114       meteorological factors (WS, WD, T, RH, P, Jvalues), gas pollutants (O<sub>3</sub>, CO, SO<sub>2</sub>, NO,  
115       NO<sub>2</sub>, HONO, HCHO, PAN), and non-methane hydrocarbons (NMHCs) are provided in  
116       Table S1.

117       The measurement of NO, NO<sub>2</sub>, O<sub>3</sub>, CO, and SO<sub>2</sub> was carried out using commercial  
118       Thermo Electron model series instruments. Thereof, NO and NO<sub>2</sub> were measured using a  
119       chemical fluorescence method (CL) with an enhanced trace-level NO-NO<sub>2</sub>-NO<sub>x</sub> analyzer  
120       (PKU-PL), which achieved a detection limit of 50 ppt (Tan et al., 2017a). The detection  
121       of O<sub>3</sub> and SO<sub>2</sub> was conducted through Thermo Electron model 49i and 43i, respectively,  
122       while Thermo Electron model 48i was utilized for CO detection. Cavity ring-down  
123       spectroscopy (CRDS, Picarro-G2401) was employed for CO detection in parallel, and  
124       another ultraviolet absorption instrument (Ecotech EC9810B) was for ozone detection.  
125       The instrument inlets were placed within 5 meters of each other for comparison.

126       To ensure measurement accuracy, the instruments in the campaign underwent zero  
127       point calibration procedures during the early (August 31st) and late (September 21st)  
128       observation periods, and cross-calibrations for O<sub>3</sub> and CO measurements were carried out  
129       during the middle (September 9th). Furthermore, additional zero calibration for Thermo  
130       48i CO detection was undertaken daily from 0:00-0:30 to minimize shift correction. The  
131       comparison results revealed high consistency within the instrument accuracy range for  
132       both CO and O<sub>3</sub> measurements (Fig. S2(a)(b)).

133       HONO was detected using a home-built instrument by cavity-enhanced absorption  
134       spectroscopy (CEAS), while formaldehyde was determined by the Hantzsch method  
135       (SDL MODEL 4050) (Duan et al., 2018; Yang et al., 2021a). An automated gas  
136       chromatograph equipped with a mass spectrometer and flame ionization detector  
137       (GC-FID/MS) was employed for the online measurement of 99 VOCs species.  
138       Information table for parts of the VOC monitoring species by online GC-MS/FID was  
139       listed in Table S2.

140       The eight crucial photolysis frequencies (j(NO<sub>2</sub>), j(H<sub>2</sub>O<sub>2</sub>), j(HCHO\_M), j(HCHO\_R),

141  $j(\text{HONO})$ ,  $j(\text{NO}_3\text{ M})$ ,  $j(\text{NO}_3\text{ R})$ ,  $j(\text{O}^1\text{D})$ ) were directly measured by a photolysis  
142 spectrometer (Metcon, Germany). The unmeasured photolysis frequencies of the  
143 remaining active species were computed using Eq.(1):

$$j = l \cdot \cos(\chi)^m \cdot e^{-n \cdot \sec(\chi)} \quad (1)$$

144 The variations in photolysis frequency due to solar zenith angle ( $\chi$ ) were adjusted based  
145 on the ratio of observed and simulated  $j(\text{NO}_2)$ . The optimal values for parameters ( $l$ ,  $m$ ,  
146 and  $n$ ) for different photolysis frequencies were extensively detailed by the MCM v3.3.1  
147 ([http://mcm.york.ac.uk/parameters/photolysis\\_param.htm](http://mcm.york.ac.uk/parameters/photolysis_param.htm)) (Jenkin et al., 2003; Jenkin et  
148 al., 1997).

## 149 **2.2 Radical measurement**

### 150 **2.2.1 OH, HO<sub>2</sub>, RO<sub>2</sub> Concentrations**

151 The laser-induced fluorescence instrument developed by the Anhui Institute of Optics  
152 and Fine Mechanics (AIOFM-LIF) was used to simultaneously detect the concentrations  
153 of OH, HO<sub>2</sub>, and RO<sub>2</sub> radicals, along with OH reactivity ( $k_{\text{OH}}$ ). The OH radical was  
154 directly measured by detecting on-resonance fluorescence excited by a 308 nm laser. An  
155 indirect measurement for HO<sub>2</sub> was carried out after converting it to OH at a fixed  
156 efficiency (Heard and Pilling, 2003).

157 The laser utilized for fluorescence excitation is a high-frequency tunable dye laser  
158 that emits a 308 nm laser, with the laser power divided into a ratio of 0.45:0.45:0.08:0.02.  
159 Of this power, 90% is directed towards fluorescence cells for concentration and reactivity  
160 detection via optical fibers, respectively. 8% of the laser power is directed to a reference  
161 cell, while the remaining 2% is used to monitor real-time power fluctuations. The laser is  
162 transmitted through HO<sub>2</sub>, OH, and RO<sub>2</sub> cells in turn via a coaxial optical path. Two  
163 photodiodes are set up at the end of the reference cell and RO<sub>2</sub> detection cell, respectively.  
164 The voltage signals and power fluctuations are compared synchronously to diagnose the  
165 laser stability. To maintain detection efficiency, the power inside the measurement cells  
166 should not be less than 10 mW. Sampling nozzles of 0.4 mm are deployed above OH and  
167 HO<sub>2</sub> cells for efficient sampling at a flow rate of approximately 1.1 SLM, and the  
168 pressure for all fluorescence cells are maintained at 400 Pa. The micro-channel plate  
169 (MCP) detects the weak fluorescence signal collected by lens systems with low noise and  
170 high gain. Additionally, a digital delay generator (DG645) optimizes the timing control

171 between the laser output, signal detection, and data acquisition. All of these modules are  
172 integrated into a sampling box with constant air conditioning, except for the laser.

173 The detection of RO<sub>2</sub> radicals is more complex compared to the integrated detection  
174 of OH and HO<sub>2</sub> radicals (Whalley et al., 2013). To achieve the complete chemical  
175 conversion from RO<sub>x</sub> to HO<sub>2</sub>, a crucial role is played by a 66 mm×830 mm aluminium  
176 flow tube, whose performance has been confirmed through the CHOOSE-2019 field  
177 campaign (Li et al., 2020). A mixture of 0.17% CO and 0.7 ppm NO injected into the  
178 flow tube facilitates the reduction of heterogeneous radical loss and enhancement of  
179 conversion efficiency. The sampling flow is limited to 7 SLM by a 1 mm nozzle, and the  
180 tube pressure is maintained at 25 hPa. In contrast to the HO<sub>x</sub> cells, the large-diameter  
181 nozzle (4 mm) is equipped above the cell, and a high concentration of NO (~300 ppm)  
182 facilitates the full magnitude HO<sub>2</sub>→OH conversion.

183 The observation data (H<sub>2</sub>O, O<sub>3</sub>) is combined with experimental characterization to  
184 eliminate ozone photolysis interference, and most interference signals are excluded by  
185 utilizing wavelength modulation (Zhang et al., 2022a). A comparison experiment with  
186 PKU-LIF demonstrated the consistency of OH measurement in complex atmosphere  
187 (Zhang et al., 2022b). An additional atmospheric oxidation observation was conducted in  
188 the same location and season in 2022 with a chemical modulation method to determine  
189 the chemical background of OH radicals (Fig. S3). During the ozone pollution  
190 (2022.9.29-2022.10.3), the daytime peaks of ozone concentration above 75 ppb,  
191 accompanied by alkene species approaching ~10 ppb. The diurnal concentration of  
192 isoprene was also a high level (>1 ppb). The chemical conditions are more favourable to  
193 induce OH interference than in the TROPSTECT campaign, while the OH concentrations  
194 achieved by chemical modulation (OH<sub>chem</sub>) and wavelength modulation (OH<sub>wav</sub>) were in  
195 good agreement. No obvious chemical background was observed by deploying an inlet  
196 pre-injector. Therefore, it is not expected that OH measurement in the present study was  
197 affected by internal interference.

198 For HO<sub>2</sub> measurement, lower NO concentration (~1.6 × 10<sup>12</sup> cm<sup>-3</sup>, corresponding to  
199 ~15% conversion efficiency) are selected to limit the RO<sub>2</sub>→HO<sub>2</sub> interference to less than  
200 5% (Wang et al., 2021). Since only the total-RO<sub>2</sub> mode is used for the campaign, the  
201 additional uncertainty introduced by RO<sub>2</sub>/R(OH)O<sub>2</sub> classification is negligible (Tan et al.,

202 2017b). The observed maximum daily PAN (11:00-14:00) is only  $1.15 \pm 0.67$  ppb,  
203 resulting in a calculated PAN-pyrolytic interference for  $\text{RO}_2$  measurement of less than 1  
204 ppt (Fuchs et al., 2008). The general applicability of AIOFM-LIF in complex atmosphere  
205 has been demonstrated through various campaigns (Zhang et al., 2022b; Wang et al.,  
206 2021; Wang et al., 2019a).

207 To complete the calibration task, a standard source stably generates equal amounts  
208 of OH and  $\text{HO}_2$  radicals (Wang et al., 2020). The radical source is also capable of  
209 yielding specific  $\text{RO}_2$  by titrating hydrocarbon with OH. It is noteworthy that  $\text{CH}_3\text{O}_2$  has  
210 the highest mixing ratio in the  $\text{RO}_2$  species, thus it was chosen to represent for sensitivity  
211 calibration. The instrument is calibrated every two days, except during rainy weather. The  
212 limit of detection (LOD) for OH,  $\text{HO}_2$ , and  $\text{RO}_2$  in different cells with a typical laser  
213 power of 10 mW is measured at  $3.3 \times 10^5 \text{ cm}^{-3}$ ,  $1.1 \times 10^6 \text{ cm}^{-3}$ , and  $2.5 \times 10^6 \text{ cm}^{-3}$ ,  
214 respectively (60 s,  $1\sigma$ ). Measurement accuracy for OH,  $\text{HO}_2$ , and  $\text{RO}_2$  radicals are  
215 reported to be 13%, 17%, and 21%, respectively.

### 216 **2.2.2 OH reactivity( $k_{\text{OH}}$ )**

217 The detection of  $k_{\text{OH}}$  in the atmosphere, defined as the reciprocal of OH lifetime, was  
218 conducted using a laser flash photolysis laser-induced fluorescence (LP-LIF) instrument  
219 (Lou et al., 2010). The configuration structure for  $k_{\text{OH}}$  measurement has been detailed in a  
220 previous study(Liu et al., 2019). The flow tube in the OH production-reaction unit is at  
221 ambient pressure, with a gas flow rate of 17 SLM. A pulsed laser beam (266 nm with an  
222 average power of 15 mJ) is output from a frequency-quadrupled Nd:YAG laser, which  
223 generates stable OH radical through flash photolysis of ambient ozone in the flow tube.  
224 Consistent and stable production of OH radicals is ensured by maintaining a stable  
225 concentration of reactants, flow field, and laser energy. Under conditions of 80 ppb  $\text{O}_3$   
226 and 8000 ppm water vapor concentration, OH radicals produced in the flow tube remains  
227 at the concentration order of  $10^9 \text{ cm}^{-3}$ . Subsequently, the OH radicals are sampled through  
228 a nozzle into a fluorescence cell. The OH fluorescence signal is then detected using laser  
229 pump and probe techniques and is fitted to calculate the slope of OH decay ( $k_{\text{OH}}$ ). The  
230 detection accuracy, achieved with an integration time of 180 s, is  $0.3 \text{ s}^{-1}$  ( $1\sigma$ ).

### 231 **2.3 Observation-Based Model**

232 The Regional Atmospheric Chemical Mechanism version 2 (RACM2) incorporating

233 the latest Leuven isoprene mechanism (LIM) was utilized to simulate the concentrations  
 234 and reactions of OH, HO<sub>2</sub>, and RO<sub>2</sub> radicals (Stockwell et al., 1997; Griffith et al., 2013;  
 235 Peeters et al., 2014). The RACM2-LIM1 mechanism was specifically involved with  
 236 fewer species compared to the explicit MCM mechanism, thus ensuring higher  
 237 operational efficiency (Liu et al., 2022). The comprehensive list of model constraints was  
 238 provided in Table S3. The measured NMHCs include 29 alkanes, 11 alkenes, 15  
 239 aromatics, as well as acetylene and isoprene. For the base scenario, boundary conditions  
 240 were established using the observed species, with assumed concentrations of hydrogen  
 241 (H<sub>2</sub>) and methane (CH<sub>4</sub>) at 550 ppb and 1900 ppb, respectively. An ozone-simulation test  
 242 was conducted to determine the suitable atmospheric lifetime ( $\tau_D$ ) for the base model. At  
 243 the lifetime of 24 hours, with a corresponding first-order loss rate of 1.1 cm/s (assuming a  
 244 boundary layer height of 1 km), the simulated ozone concentration closely matched the  
 245 observed values (Fig. S4). To improve the model-measurement consistency between OH,  
 246 HO<sub>2</sub> and RO<sub>2</sub> radicals, a series of sensitivity analyses were performed to evaluate the  
 247 impacts of potential mechanisms, as detailed in Table 1. The time resolution of all  
 248 constraints was uniformly set to 15 minutes through averaging or linear interpolation. To  
 249 reinitialize unconstrained species to a steady-state, three days of data were input in  
 250 advance as the spin-up time.

251 **Table 1.** The sensitive test scenarios utilized to improve the model-measurement consistency between  
 252 OH, HO<sub>2</sub> and RO<sub>2</sub> radicals.

Scenario	Configuration	Purpose
Base	RACM2 updated with isoprene reaction scheme (LIM)	The base case with the species involved in Table S3 are constrained as boundary conditions.
X on	As the base scenario, but add the X mechanism, and the X level is between 0.25 - 0.5 ppb.	To untangle the missing OH source where base scenario failed.
MTS on	As the base scenario, but add a monoterpene source, and the monoterpene level is ~0.4 ppb.	Utilizing monoterpene-derived RO <sub>2</sub> to represent the alkoxy radicals with rather complex chemical structures.
MTS+X on	As the base scenario, but both the X mechanism and monoterpene source are considered.	To consider both the missing OH and RO <sub>2</sub> sources.
HAM on	As the base scenario, but add the reactive aldehyde chemistry.	To provide a test of whether the proposed mechanism can explain the missing OH source.
HAM on (4 × ALD)	As the base scenario, but add the reactive aldehyde chemistry, and the concentration of ALD was amplified by a factor of 4.	To quantify the impact of missing aldehyde primary emissions on RO <sub>x</sub> chemistry.
Ozone simulation	As the base scenario, but remove the constraints of the observed ozone and NO concentrations.	To test the suitable lifetime for the base model.
HCHO simulation	As the base scenario, but remove the constraint of the observed HCHO concentration.	To test the simulation effect of the existing mechanism on formaldehyde

concentration.

---

253

254 The local formation of ozone can be accurately quantified through the online  
255 measurement of ROx radicals (Tan et al., 2018). To overcome the interference from NO,  
256 the total oxidant (Ox), which is defined as the sum of NO<sub>2</sub> and O<sub>3</sub>, can serve as a reliable  
257 parameter to indicate the level of oxidation. Eq.(2) shows that the rate of NO oxidation  
258 by peroxy radicals is equivalent to the production of O<sub>3</sub>, denoted as F(Ox):

259 
$$F(O_x) = k_{HO_2+NO}[NO][HO_2] + \sum_i k_{RO_2^i+NO}[NO]RO_2^i \quad (2)$$

260 The major loss pathways for Ox encompass ozone photolysis, ozonolysis reactions,  
261 and radical-related reactions (OH/HO<sub>2</sub>+O<sub>3</sub>, OH+NO<sub>2</sub>), represented as D(Ox) in Eq.(3):

262 
$$D(O_x) = \varphi_{OH}j(O^1D)[O_3] + \sum_i \{\varphi_{OH}^i k_{Alkenes+O_3}^i [Alkenes][O_3]\} + (k_{O_3+OH}[OH] +  
263 k_{O_3+HO_2}[HO_2])[O_3] + k_{OH+NO_2}[OH][NO_2] \quad (3)$$

264 Here, the OH yields from ozone photolysis and ozonolysis reactions are denoted as  $\varphi_{OH}$   
265 and  $\varphi_{OH}^i$ , respectively.

266 The net photochemical Ox production rate in the troposphere, denoted as P(Ox) in  
267 Eq.(4), can therefore be calculated as the difference between Eqs. (2) and (3):

268 
$$P(O_x) = F(O_x) - D(O_x) \quad (4)$$

## 269 2.4 Experimental budget analysis

270 In this study, an experimental radical budget analysis was also conducted (Eqs. (5)  
271 - (12)). Unlike model studies, this method relies solely on field measurements  
272 (concentrations and photolysis rates) and chemical kinetic data, without depending on  
273 concentrations calculated by models(Whalley et al., 2021; Tan et al., 2019b). Given the  
274 short-lived characteristics of OH, HO<sub>2</sub>, and RO<sub>2</sub> radicals, it is expected that the  
275 concentrations are in a steady state, with total production and loss rates being  
276 balanced(Lu et al., 2019a). By comparing the known sources and sinks for radicals,  
277 unknown processes for initiation, transformation and termination can be determined.

$$P(OH) = j_{HONO}[HONO] + \varphi_{OH}j(O^1D)[O_3] + \sum_i \{\varphi_{OH}^i k_{Alkenes+O_3}^i [Alkenes][O_3]\} + (k_{HO_2+NO}[NO] + k_{HO_2+O_3}[O_3])[HO_2] \quad (5)$$

$$D(OH) = [OH] \times k_{OH} \quad (6)$$

$$\begin{aligned}
P(HO_2) = & 2 \times j_{HCHO\_R}[HCHO] + \Sigma i \{ \varphi_{HO_2}^i k_{Alkenes+O_3}^i [Alkenes][O_3] \} \\
& + (k_{HCHO+OH}[HCHO] + k_{CO+OH}[CO])[OH] \\
& + \alpha k_{RO_2+NO}[NO][RO_2]
\end{aligned} \tag{7}$$

$$\begin{aligned}
D(HO_2) = & (k_{HO_2+NO}[NO] + k_{HO_2+O_3}[O_3] + k_{HO_2+RO_2}[RO_2] \\
& + 2 \times k_{HO_2+HO_2}[HO_2])[HO_2]
\end{aligned} \tag{8}$$

$$\begin{aligned}
P(RO_2) = & \Sigma i \{ \varphi_{RO_2}^i k_{Alkenes+O_3}^i [Alkenes][O_3] \} \\
& + k_{OH}[VOCs][OH]
\end{aligned} \tag{9}$$

$$\begin{aligned}
D(RO_2) = & \{(\alpha + \beta)k_{RO_2+NO}[NO] + (2 \times k_{RO_2+RO_2}[RO_2] \\
& + k_{HO_2+RO_2}[HO_2])[RO_2]
\end{aligned} \tag{10}$$

$$\begin{aligned}
P(RO_x) = & \Sigma i \{ (\varphi_{OH}^i + \varphi_{HO_2}^i + \varphi_{RO_2}^i) k_{Alkenes+O_3}^i [Alkenes][O_3] \} + j_{HONO}[HONO] \\
& + \varphi_{OH} j(O^1D)[O_3] + 2 \times j_{HCHO\_R}[HCHO]
\end{aligned} \tag{11}$$

$$\begin{aligned}
D(RO_x) = & (k_{OH+NO_2}[NO_2] + k_{OH+NO}[NO])[OH] + \beta k_{RO_2+NO}[NO] \\
& + 2 \times (k_{RO_2+RO_2}[RO_2][RO_2] + k_{HO_2+RO_2}[HO_2][RO_2] \\
& + k_{HO_2+HO_2}[HO_2][HO_2])
\end{aligned} \tag{12}$$

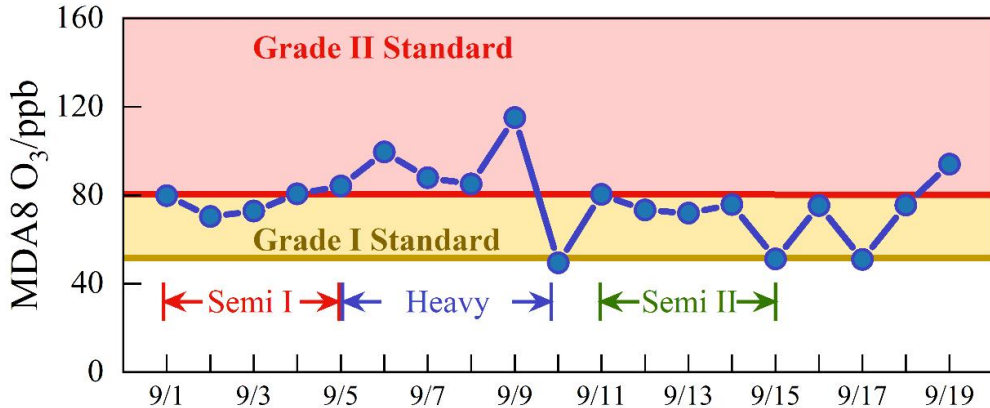
278 In which,  $j(HONO)$ ,  $j(O^1D)$  are the measured photolysis rates of HONO and  $O_3$ ,  
279 respectively, and  $j_{HCHO\_R}$  is the measured photolysis rate for the channel of  
280 formaldehyde photolysis generating  $HO_2$ .  $\varphi_{OH}$  represent the OH yield in the  $O_3$   
281 photolysis reaction.  $\varphi_{OH}^i$ ,  $\varphi_{HO_2}^i$  and  $\varphi_{RO_2}^i$  are the yields for the ozonolysis reaction  
282 producing OH,  $HO_2$ , and  $RO_2$ , respectively.  $\alpha$  is the proportion of  $RO_2$  radicals reacting  
283 with NO that are converted to  $HO_2$ , and  $\beta$  is the proportion of alkyl nitrates formation,  
284 which are set to 1 and 0.05, respectively(Tan et al., 2019b).

## 285 3 Results

### 286 3.1 Overview of Measurement

287 During the observation period, the meteorological parameters and trace gas  
288 concentrations were plotted in Fig. S5. The timeseries revealed that the peak temperature  
289 exceeded 30°C, and the humidity levels remained between 30 – 50% during the daytime.  
290 The photolysis rates were observed to peak at noon (11:00 – 13:00), with  $j(O^1D)$  and  
291  $j(NO_2)$  reaching approximately  $3 \times 10^{-5} \text{ s}^{-1}$  and  $8 \times 10^{-3} \text{ s}^{-1}$ , respectively. Brief rainfall events  
292 temporarily happened on September 10th, 15th, and 17th, but totally favorable  
293 meteorologies induced the prolonged ozone pollution. The daily maximum 8-hour

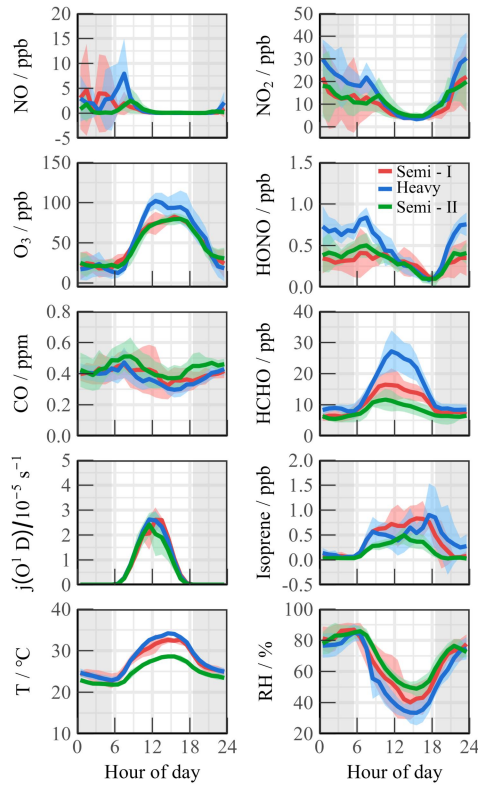
294 average ozone concentration (MDA8), as depicted in Fig. 2, consistently exceeded the  
 295 Chinese Grade I national air quality standard (GB3095-2012) throughout the observation,  
 296 with nine days exceeding the Grade II standard.



297  
 298 **Fig. 2.** The daily maximum 8 h average  $O_3$  during the campaign. The yellow and red lines denote the Grade I and  
 299 Grade II national standards for  $O_3$ , respectively. Brief rainfall events temporarily happened on 10, 15, and 17 Sep.

300 The ozone pollution can be categorized into three continuous periods based on  
 301 pollution levels, which disclose transitional ‘Semi - Heavy - Semi’ pollution  
 302 characteristics. Fig. 3 depicts daily variations in meteorological and trace gas  
 303 concentrations for different periods. During the Semi I (1 to 5 September) and Semi II (11  
 304 to 14 September) periods, the MDA8 levels exceeded Grade I standard, with an average  
 305 value of  $75.92 \pm 5.14$  ppb and  $75.45 \pm 3.73$  ppb, respectively. Notably, NO levels peaked  
 306 around 9:00 and rapidly decreased to a few hundred ppt due to photochemistry. In  
 307 addition, HONO and NO<sub>2</sub> exhibited bimodal variations, with diurnal concentration ranges  
 308 of 0.09 – 0.50 ppb and 3.35 – 13.77 ppb, respectively. The HONO/NO<sub>2</sub> ratios during both  
 309 Semi periods were consistent with previous urban/suburban observations, with daytime  
 310 values of  $0.049 \pm 0.014$  and  $0.035 \pm 0.012$ , respectively (Yang et al., 2021b; Shi et al., 2020;  
 311 Hu et al., 2022). Isoprene levels accumulated during the day and decreased at night  
 312 during both Semi pollution episodes, with a diurnal average concentration in Semi II only  
 313 49.3% of that in Semi I ( $0.71 \pm 0.087$  ppb vs  $0.35 \pm 0.073$  ppb). Formaldehyde, as the key  
 314 oxidation species, exhibited a concentration profile mirroring that of isoprene, with  
 315 significantly higher concentrations ranging from 1.20 to 36.34 ppb compared to other  
 316 urban regions (Ma et al., 2022; Yang et al., 2022; Tan et al., 2017b; Yang et al., 2021a).  
 317 Heavy pollution episodes from 5 to 9 September resulted in daytime ozone concentration  
 318 as high as 129.9 ppb, and oxidation-related species such as HCHO, HONO, NO<sub>x</sub>, and

319 VOCs increased synchronously compared to other days.



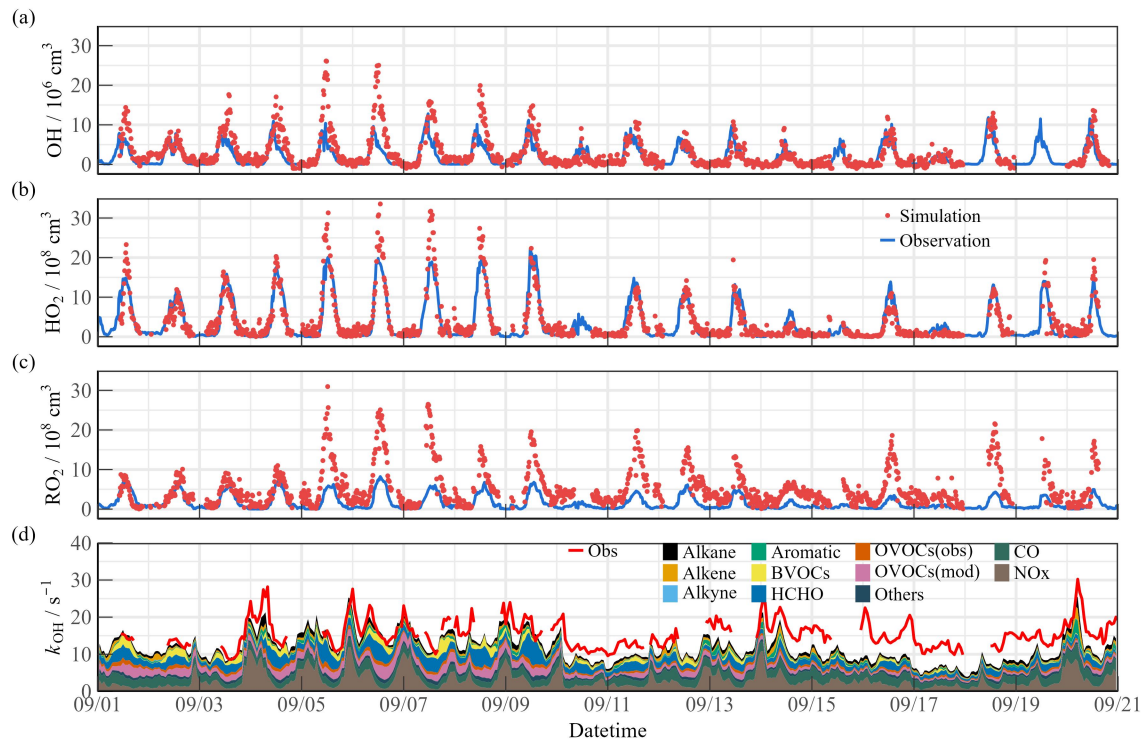
320

321 **Fig. 3.** Mean diurnal profiles of observed meteorological and chemical parameters during the campaign. Three periods  
322 were divided for subsequent study (Semi I, Heavy, and Semi II).

### 323 **3.2 ROx radical concentrations and budgets**

324 The observed and modeled timeseries for OH, HO<sub>2</sub>, RO<sub>2</sub>, and *k*<sub>OH</sub> during the  
325 observation time are depicted in Fig. 4. The diurnal peaks of radicals exhibited a wide  
326 span due to changes in environmental conditions, with ranges of  $3.6 - 27.1 \times 10^6 \text{ cm}^{-3}$  for  
327 OH,  $2.1 - 33.2 \times 10^8 \text{ cm}^{-3}$  for HO<sub>2</sub>, and  $4.9 - 30.5 \times 10^8 \text{ cm}^{-3}$  for RO<sub>2</sub>. Continuous data for  
328 *k*<sub>OH</sub> observation were acquired within a range of  $8.6 - 30.2 \text{ s}^{-1}$ . Fig. S6 presents the  
329 diurnal profiles of the observed and modeled values during different episodes. The  
330 diurnal maximum of OH radical at noon differed between Semi I and Semi II, with  
331  $9.28 \times 10^6 \text{ cm}^{-3}$  and  $5.08 \times 10^6 \text{ cm}^{-3}$ , respectively, while total peroxy radicals (HO<sub>2</sub>+RO<sub>2</sub>)  
332 remained at similar levels with  $19.43 \times 10^8 \text{ cm}^{-3}$  and  $18.38 \times 10^8 \text{ cm}^{-3}$ . Additionally, the  
333 distribution of peroxy radicals are not similar in the two Semi periods, with HO<sub>2</sub>/RO<sub>2</sub>  
334 ratios of 1.69:1 and 0.76:1, respectively, which reflects the uneven oxidation levels  
335 between Semi I and Semi II. During the Heavy ozone pollution, the averaged OH, HO<sub>2</sub>,  
336 and RO<sub>2</sub> concentrations were 1.90, 2.15, and 1.98 times higher than those in the Semi

337 periods, suggesting a stronger oxidation capacity, with  $k_{OH}$  in Heavy being 26.43% and  
 338 9.56% higher than in Semi I and Semi II, respectively. Limited anthropogenic emissions  
 339 in the suburban environment reduced the oxidation contribution by NOx and CO  
 340 (27.59%). During the heavy pollution, organic species exhibited dominant behavior  
 341 regarding diurnal reactivity (9.22  $s^{-1}$  for 69.79%), and anthropogenic hydrocarbons were  
 342 not major  $k_{OH}$  sources. With an abundant level (~1 ppb), isoprene contributed more than  
 343 10% of the reactivity in the diurnal cycle. Therefore, the effect of BVOCs species (such  
 344 as monoterpenes, limonene, etc.) on radical chemistry cannot be ignored (Ma et al., 2022;  
 345 Wang et al., 2022b).  $k_{OVOCs}$  are categorized into three groups:  $k_{OVOCs(Obs)}$ ,  $k_{OVOCs(Model)}$ , and  
 346  $k_{HCHO}$ . Given the significance of formaldehyde photolysis, the contribution of HCHO to  
 347  $k_{OVOCs}$  is distinguished.  $k_{OVOCs(Obs)}$  encompasses species observed in addition to  
 348 formaldehyde, such as acetaldehyde (ACD) and the oxidation products of isoprene  
 349 (MACR and MVK). Intermediates generated by the model, including glyoxal (GLY),  
 350 methylglyoxal (MGLY), higher aldehydes (ALD), ketones (KET), methyl ethyl ketone  
 351 (MEK), and methanol (MOH), are classified as  $k_{OVOCs(Model)}$ . Upon considering  
 352  $k_{OVOCs(Model)}$ , the reactivity calculated prior to September 10th aligns quite well with the  
 353 observed OH reactivity.



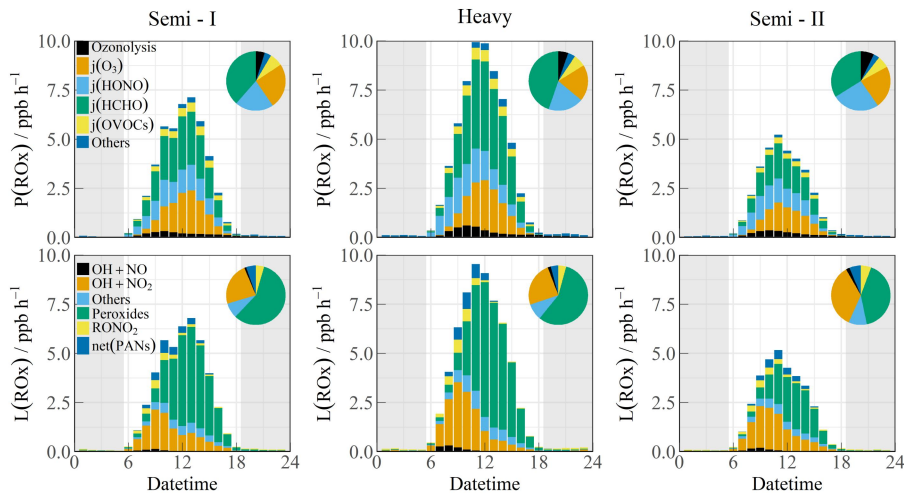
354

**Fig. 4.** Timeseries of the observed and modelled parameters for OH, HO<sub>2</sub> and  $k_{OH}$  during the observation period. (a) OH, (b) HO<sub>2</sub>, (c)  $k_{OH}$ .

The significant variations in oxidation can be inferred from the disparities during different pollution periods (Fig. S6). During Semi I, there was a good agreement between the measurement and model for peroxy radicals during the daytime. The RACM2-LIM1 mechanism effectively replicated the morning OH radical concentration. However, following 10:00, NO gradually declined, and the increasing OH concentration could not be accounted for by the  $\text{HO}_2+\text{NO}$  formation channel, resulting in a maximum underestimation of  $5.85 \times 10^6 \text{ cm}^{-3}$  (Hofzumahaus et al., 2009; Lu et al., 2012). In the Semi II episode, OH was not underestimated in the low-NO regime, with a slight overestimation of  $\text{HO}_2$  concentration. However, the simulated  $\text{RO}_2$  concentration was only  $3.78 \times 10^8 \text{ cm}^{-3}$ , whereas observations were 2.77 times larger than the simulation, indicating the existence of additional reaction pathways that likely propagated the  $\text{OH} \rightarrow \text{RO}_2$  conversion efficiency. A significant discrepancy of radicals existed in the heavy ozone concentration, with OH,  $\text{HO}_2$ , and  $\text{RO}_2$  radicals concurrently underestimated at noon by  $8.23 \times 10^6 \text{ cm}^{-3}$ ,  $3.94 \times 10^8 \text{ cm}^{-3}$  and  $11.59 \times 10^8 \text{ cm}^{-3}$ , respectively. The observed  $\text{HO}_2/\text{RO}_2$  ratio approached 1:1, while the model reflected an unreasonable ratio of 3:1, indicating deficiencies in both primary sources and secondary propagation. The calculated reactivity seems to compare well with the observed OH reactivity at the start of the measurement period, but then there is evidence of missing OH reactivity after September 10th (Fig. 4(d)). Due to the limitations of available instruments, this observation only measured a limited number of OVOCs species, making it difficult to accurately quantify the contribution of larger aldehydes and ketones, carboxylic acids, nitrophenols, and other multifunctional species to  $k_{\text{OH}}$  (Wang et al., 2024). Since the MCM mechanism considers more secondary formation reactions than the RACM2 mechanism, it can qualitatively assess the photochemical role of unmeasured OVOCs species in the atmosphere (Wang et al., 2022d). The additional modeled OVOCs by the MCM v3.3.1 mechanism contributed  $\sim 2.4 \text{ s}^{-1}$  to the missing OH reactivity (Fig. S7). During Heavy period, the reactivity of more model oxidation products increased the daytime  $k_{\text{OH}}$  by about  $5.1 \text{ s}^{-1}$ . Therefore, the observed  $k_{\text{OH}}$  can serve as an upper limit for sensitivity tests, thereby the full suite of radical measurement can be performed to explore the missing oxidation properties and ozone formation (Section 4.1).

387 Fig. 5 displays the diurnal profiles of the ROx budget during different episodes. In  
 388 Semi I, formaldehyde photolysis showed a higher contribution (38.6%), while HONO  
 389 photolysis (21.0%) and ozone photolysis (24.7%) accounted for similar proportions in  
 390 primary sources. The contribution of photolysis from other OVOCs was comparable to  
 391 that of ozonolysis reactions (7.2% vs. 4.8%). However, in Semi II, the decreased  
 392 oxidation level was attributed to lower ROx sources, despite the similar proportions.  
 393 During the Heavy period, the primary sources dramatically increased (up to ~10 ppb/h),  
 394 with HCHO photolysis contributing the most, alongside other sources at common levels  
 395 (ranging between 1.74 – 2.66 ppb/h) in the YRD region (Ma et al., 2022). Fast HCHO  
 396 oxidation dominated the radical primary source during heavy ozone pollution, which  
 397 contrasts with the dominant role of HONO/O<sub>3</sub> in other megacities (Yang et al., 2022; Tan  
 398 et al., 2017b; Yang et al., 2021a).

399 The radical removal rate during the daytime was generally balanced with production  
 400 contributions. In the morning, owing to high NOx concentrations, radical termination was  
 401 mainly dominated by OH+NO<sub>2</sub>, OH+NO, RO<sub>2</sub>+NO, and RO<sub>2</sub>+NO<sub>2</sub>. Furthermore, the  
 402 formation of peroxy nitrate accounted for a certain proportion (~5%). As NOx  
 403 concentrations decreased after 10:00, self-reactions in peroxy radicals became significant.



404  
 405 **Fig. 5.** The diurnal profiles of ROx budget during different polluted episodes (Semi I, Heavy, and Semi II). The  
 406 pie chart denotes proportions in different parts during the daytime (10:00-15:00). The grey areas denote nighttime.  
 407

408 By comparing the known sources and sinks for radicals, unknown processes for  
 409 initiation, transformation and termination can be determined in the experimental budget  
 410 analysis (Fig. S8). During the Semi I period, the production and destruction rates of HO<sub>2</sub>,  
 RO<sub>2</sub>, and total ROx radicals were very consistent, but a significant lack of a source term

411 for OH radicals was existed after 10:00. This missing source became more pronounced  
412 during the Heavy period, reaching 16 ppb/h at noon, which is close to the results  
413 observed by AIRPRO, but three times that observed by Heshan in PRD region(Tan et al.,  
414 2019b; Whalley et al., 2021). The ratio of OH production-to-destruction rate during the  
415 Semi II period was close to 1, indicating consistency between the observed results of OH,  
416 HO<sub>2</sub>, *k*<sub>OH</sub>, and other precursors(Whalley et al., 2018). However, the generation of HO<sub>2</sub>  
417 radicals in the morning was about twice as high as the removal rate, suggesting that there  
418 are contributions from unconsidered HO<sub>2</sub> radical removal channels (such as  
419 heterogeneous reactions)(Song et al., 2021). During the Heavy period, there was a rapid  
420 total removal rate of RO<sub>2</sub> radicals, reflecting the dominated HO<sub>2</sub> generation by the  
421 reaction of RO<sub>2</sub> radicals with NO. Although the P(HO<sub>2</sub>) and D(HO<sub>2</sub>) were quite in  
422 balance, the removal rate of RO<sub>2</sub> radicals far exceeded the known production rate  
423 (especially before 12:00). Previous work has shown that halogen chemistry (such as  
424 photolysis of nitryl chloride (ClNO<sub>2</sub>)) could be an important source in the morning time,  
425 but this was not included in the calculation of ROx or RO<sub>2</sub> budget in this campaign(Tan  
426 et al., 2017b). The steady-state analysis for HO<sub>2</sub> radical in the London campaign  
427 emphasized that only by significantly reducing the observed RO<sub>2</sub>-to-HO<sub>2</sub> propagation  
428 rate to just 15% could balance both P(HO<sub>2</sub>) and D(HO<sub>2</sub>), indicating that the RO<sub>2</sub>-related  
429 mechanism for propagation to other radical species may not be fully understood(Whalley  
430 et al., 2018). Therefore, based on the current knowledge seems unlikely to explain the  
431 required source-sink difference of nearly 25 ppb/h in the RO<sub>2</sub> budget. Sensitivity analysis  
432 is needed to further infer the causes of the difference for the experimental budget  
433 analysis.

### 434 3.3 Oxidation comparison

435 The concentration of OH radicals during the daytime is a crucial indicator of  
436 atmospheric oxidation levels (Liu et al., 2021). Table 2 summarized radicals and related  
437 parameters for regions with similar latitudes ( $32.0^\circ \pm 2^\circ$  N,  $j(O^1D) \approx 2.5 \pm 0.5 \times 10^{-5} \text{ s}^{-1}$ ).  
438 The joint influence of solar radiation and local photochemistry resulted in megacities  
439 exhibiting intense oxidation levels in summer/autumn, characterized by OH radicals  
440 being maintained at approximately  $10.0 \times 10^6 \text{ cm}^{-3}$  at noon. Notably, an observation in  
441 Houston revealed an OH concentration of nearly  $20.0 \times 10^6 \text{ cm}^{-3}$ , with *k*<sub>OH</sub> of  $10 \text{ s}^{-1}$  (Mao

442 et al., 2010). In areas such as Los Angeles, Pasadena, and Tokyo, the propagation  
 443 efficiency of radicals was restricted due to fresh anthropogenic emissions. OH  
 444 concentrations were only half of those observed in other megacities, with higher  
 445 inorganic-dominated  $k_{OH}$  recorded (Pasadena,  $\sim 20 \text{ s}^{-1}$ ) (George et al., 1999; Griffith et al.,  
 446 2016; Yugo Kanaya et al., 2007). In the TROPSTECT observation, the observed  $k_{OH}$   
 447 exceeded the mean value at the same latitude ( $> 15 \text{ s}^{-1}$ ). Additionally, during the Heavy  
 448 episode, higher OH concentration ( $13.5 \times 10^6 \text{ cm}^{-3}$ ) was found, comparable to the highest  
 449 level at regions with similar latitude (Houston 2000/2006, (Mao et al., 2010)).  
 450 Synchronous elevation in radical concentration and reactivity indicated a strong oxidation  
 451 level in the YRD region.

452 The observations in the YRD region showed a stable conversion factor (OH- $j(O^1D)$ )  
 453 of  $4 \pm 1 \times 10^{11} \text{ cm}^{-3} \text{ s}$ , which was comparable to other megacities in the PRD, NCP, and  
 454 SCB regions (Ma et al., 2022; Tan et al., 2019a). The corresponding slope between OH  
 455 concentration and solar radiation was used to quantify the oxidation efficiency from  
 456 photolysis, and it was observed that a higher slope of  $5.3 \times 10^{11} \text{ cm}^{-3} \text{ s}$  during the Heavy  
 457 period indicated an active radical chemistry. This implies that there is a strong oxidation  
 458 efficiency from photolysis in the YRD region.

459 During summer and autumn seasons, photochemical pollution is a common  
 460 occurrence, as noted by (Tan et al., 2021). Analysis of radical concentration across  
 461 different regions reveals that the YRD region exhibited concentrations higher than  $10^7$   
 462  $\text{cm}^{-3}$ , slightly lower than in Guangzhou in 2006 but consistent with observations in other  
 463 megacities (Ma et al., 2022; Tan et al., 2017a; Lu et al., 2012; Yang et al., 2021a).  
 464 Conversely, winter is characterized by haze pollution (Ma et al., 2019). An urban site in  
 465 Shanghai reported a peak OH concentration of  $2.6 \times 10^6 \text{ cm}^{-3}$ , closely resembling the  $1.7 -$   
 466  $3.1 \times 10^6 \text{ cm}^{-3}$  range found in polluted winter atmospheres (Zhang et al., 2022a). Although  
 467 no significant regional disparities in oxidation levels were detected in agglomerations,  
 468 attention should be directed to the YRD region due to its elevated radical concentration,  
 469 reactivity, and photolysis efficiency, signaling the need to investigate its role in radical  
 470 chemistry.

471 **Table 2.** Summary of radical concentrations and related species concentrations at regions with similar latitude and  
 472 megapolitan areas in China. All data are listed as the average in noontime (11:00~13:00).

Location	Latitude	Year	$\text{OH}$ ( $10^6 \text{ cm}^{-3}$ )	$k_{OH}$ ( $\text{s}^{-1}$ )	$j(O^1D)$ ( $10^{-5} \text{ s}^{-1}$ )	Slope ( $10^{11} \text{ cm}^{-3} \text{ s}$ )	X (ppb)	References
----------	----------	------	---	---------------------------------	---	--	------------	------------

Regions with similar latitude								
Los Angeles	34.1° N	Sep 1993	6.0	-	-	-	-	(George et al., 1999)
Nashville	36.2° N	Jun–Jul 1999	10.0	10.2	3.0	3.3 <sup>c</sup>	-	(Martinez et al., 2003)
Houston	29.7° N	Aug 2000	20.0	9.0 <sup>b</sup>	3.0	6.7 <sup>c</sup>	-	(Mao et al., 2010)
Tokyo	35.6° N	Jul–Aug 2004	6.3	-	2.5	3.0	-	(Yugo Kanaya et al., 2007)
Houston	29.7° N	Sep 2006	15.0	11.0	3.1	5.0 <sup>c</sup>	-	(Mao et al., 2010)
Pasadena	34.1° N	May–Jun 2010	4.0	20.0	2.5	1.6 <sup>c</sup>	-	(Griffith et al., 2016)
Taizhou	32.6° N	May–Jun 2018	10.6	10.8 <sup>a</sup>	2.1	4.8	0.10	(Ma et al., 2022)
Chengdu	30.7° N	Aug 2019	10.0	8.0	2.2	4.1	0.25	(Yang et al., 2021a)
TROPSTECT (Heavy)	31.9° N	Sep 2020	13.5	16.0	2.6	5.3	0.50	This work
TROPSTECT (Semi)	31.9° N	Sep 2020	7.2	14.2	2.4	3.1	0.25	This work
Regions in megapolitan areas in China								
Guangzhou (PRD)	23.5° N	Jul 2006	12.6	17.9	3.5 <sup>b</sup>	4.5	0.85	(Lu et al., 2012)
Wangdu (NCP)	38.7° N	Jun–Jul 2014	8.3	15.0	1.8	4.5	0.10	(Tan et al., 2017b)
Beijing (NCP)	39.9° N	May–Jun 2017	9.0	30.0	2.4	3.8 <sup>c</sup>	~0	(Whalley et al., 2021)
Taizhou (YRD)	32.6° N	May–Jun 2018	10.6	10.8 <sup>a</sup>	2.1	4.8	0.10	(Ma et al., 2022)
Shenzhen (PRD)	22.6° N	Sep–Oct 2018	4.5	21.0	1.8	2.4	0.10	(Yang et al., 2022)
Chengdu (SCB)	30.7° N	Aug 2019	9.0	8.0	2.2	4.0	0.25	(Yang et al., 2021a)
Hefei (YRD)	31.9° N	Sep 2020	10.4	14.3	2.4	4.4	0.30	This work

473 <sup>a</sup> The modeled  $k_{OH}$ .

474 <sup>b</sup> Value only in the afternoon.

475 <sup>c</sup> Using the ratio of OH / j(O<sup>1</sup>D)

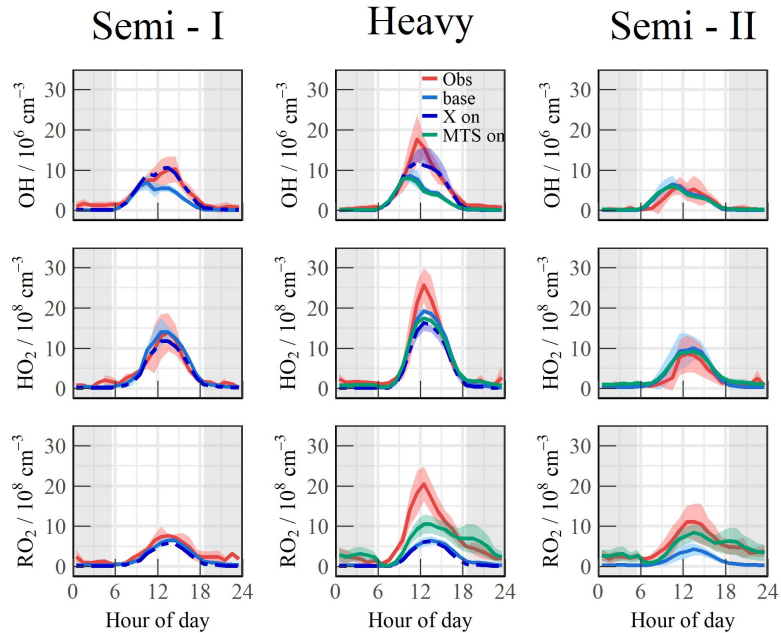
## 476 4 Discussion

### 477 4.1 Measurement–model reconciliation for radicals

#### 478 4.1.1 OH underestimation

479 Full suite of OH, HO<sub>2</sub>, RO<sub>2</sub> and  $k_{OH}$  was utilized in the TROPSTECT campaign to  
480 untangle a thorough understanding of oxidation mechanisms where base model failed.  
481 One specific phenomenon was the absence of an OH source in situations where NO  
482 levels gradually decreased after 10:00. A sensitivity test was conducted introducing a  
483 species X, analogous to NO, to enhance OH regeneration (Fig. 6, RO<sub>2</sub>→HO<sub>2</sub> and  
484 HO<sub>2</sub>→OH) (Hofzumahaus et al., 2009). It was found that the addition of as little as 0.25  
485 ppb X was sufficient to compensate for the full magnitude of the OH underestimation in  
486 the low NO region (Fig. 6). The employment of the X mechanism not only accelerated  
487 OH regeneration but also augmented the removal channel of peroxy radicals, which  
488 consequently led to a reduction in both HO<sub>2</sub> and RO<sub>2</sub> radical concentrations compared to  
489 the base scenario.

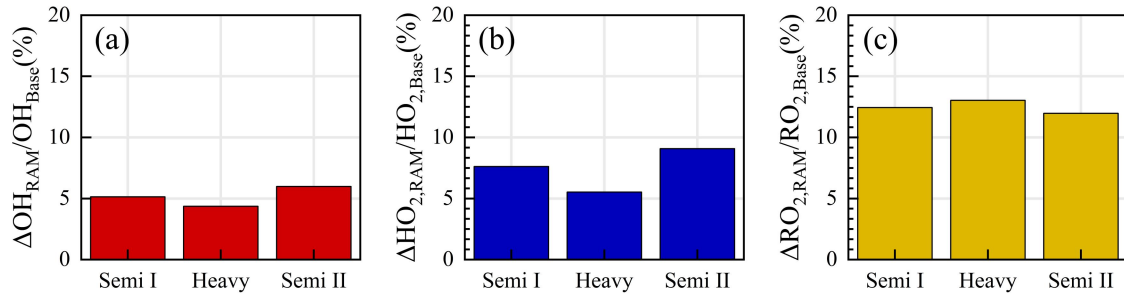
490 The underdetermined radical sources in China were corresponding to the oxidation  
 491 level (Ma et al., 2022; Tan et al., 2017a; Lu et al., 2012; Yang et al., 2021a; Wang et al.,  
 492 2019b). The required X level typically ranged from 0.1 to 0.3 ppb, with the exception of  
 493 the Backgarden observation which required 0.85 ppb X, as indicated in Table 2 (Lu et al.,  
 494 2012). A minimum limit of 0.1 ppb X was established to account for any missing  
 495 reactivity (Ma et al., 2022). Notably, throughout the entire observation, a strong  
 496 agreement between the modeled and observed OH was achieved when a mixture of 0.25  
 497 ppb X was incorporated into the base scenario, consistent with the the order of magnitude  
 498 in Chengdu (Yang et al., 2021a). During the Heavy period, the augmented  
 499 photochemistry resulted in complex oxidation, necessitating an additional missing OH  
 500 source equivalent to 0.5 ppb X to fully address the underestimation of OH.



501  
 502 **Fig. 6.** The mean diurnal profiles of measured and modeled OH, HO<sub>2</sub> and RO<sub>2</sub> concentrations at different  
 503 scenarios. Sensitivity tests included three scenarios (Scenario 1: base case; Scenario 2: X mechanism on. The dashed  
 504 line represented the performance of 0.25 ppb X introduced in the Semi I and Heavy episodes, and the blue shadow  
 505 denoted the upper limit for X influence (0.5 ppb); Scenario 3: monoterpene mechanism on; Both API and LIM were  
 506 added into the base model as upper and lower limits for the influence of monoterpene, and the mean of the two values  
 507 was taken as the average effect. The grey areas denote nighttime.

508 Missing OH sources are closely related to the chemistry of OVOCs(Yang et al.,  
 509 2024a; Qu et al., 2021). Reactive aldehyde chemistry, particularly the autoxidation of  
 510 carbonyl organic peroxy radicals (R(CO)O<sub>2</sub>) derived from higher aldehydes, is a  
 511 significant OH regeneration mechanism that has been shown to contribute importantly to  
 512 OH sources in regions with abundant natural and anthropogenic emissions during warm

513 seasons(Yang et al., 2024b). In this study, the higher aldehyde mechanism (HAM) by  
 514 Yang et al was parameterized into the base model to test new insights into the potential  
 515 missing radical chemistry (Fig. 7). The results indicate that the contribution of the HAM  
 516 mechanism to OH radicals in different episodes ranged between 4.4% - 6.0%, while the  
 517 concentrations of HO<sub>2</sub> and RO<sub>2</sub> radicals increased by approximately 7.4% and 12.5%,  
 518 respectively.



519  
 520 **Fig. 7.** The response of (a) OH, (b) HO<sub>2</sub> and (c) RO<sub>2</sub> radicals to the Higher Aldehyde Mechanism (HAM) in  
 521 different episodes (Semi I, Heavy, and Semi II) in diurnal time (10:00-15:00).

#### 522 4.1.2 RO<sub>2</sub> underestimation

523 The base scenario in Semi II is capable of accurately reproducing the concentrations  
 524 of OH and HO<sub>2</sub> radicals within the data uncertainty. However, the simulated RO<sub>2</sub>  
 525 concentration by the base model is only  $3.78 \times 10^8 \text{ cm}^{-3}$ , which does not align with the  
 526 observed oxidation levels in YRD, indicating a clear discrepancy. This underestimation is  
 527 similarly evident in the APHH observation in Beijing, as the highest observed  
 528 concentration of RO<sub>2</sub> radicals reached  $5.5 \times 10^9 \text{ cm}^{-3}$ , far exceeding the level predicted by  
 529 the MCM v3.3.1 mechanism (Whalley et al., 2021). The failure to reproduce the RO<sub>2</sub>  
 530 concentration reflects the inadequacy of the mechanisms related to RO<sub>2</sub> radicals due to  
 531 diverse oxidation reactions. This issue is further elucidated by previous studies, which  
 532 highlighted the possibility of certain VOCs undergoing more intricate isomerization or  
 533 fragmentation steps to sustain the long lifetime of RO<sub>2</sub> radicals (Whalley et al., 2018;  
 534 Whalley et al., 2021).

535 The union of  $k_{\text{OH}}$  and RO<sub>2</sub> measurement can help reveal the magnitude of missing  
 536 RO<sub>2</sub> as a hypothesis of sensitivity analysis. An additional reaction was added to the base  
 537 model in a previous research, converting OH into C96O<sub>2</sub> (the oxidation product of  
 538  $\alpha$ -pinene) with a reaction rate equal to the missing reactivity, to explore the source of the  
 539 missing RO<sub>2</sub> radicals(Whalley et al., 2021). Discrepancy of OH reactivity ( $\sim 3 - 5 \text{ s}^{-1}$ )

540 between measurement and model suggested that an additional driving force was  
541 necessary to complete the OH to RO<sub>2</sub> step. In the TROPSPECT campaign, approximately  
542 0.4 ppb of monoterpene was introduced into the base scenario as the chemical reactions  
543 of complex alkoxy radicals, which is similar to an atmospheric level in the  
544 EXPLORE-2018 campaign, the YRD region (Wang et al., 2022b). The RACM2  
545 mechanism identified  $\alpha$ -pinene (API) and limonene (LIM) as representative  
546 monoterpene species. Sensitivity tests were conducted by incorporating API and LIM  
547 into the 'MTS on' and 'MTS+X on' scenarios, respectively (Ma et al., 2022). The mean of  
548 these values was considered the average effect of monoterpene chemistry, and depicted  
549 as the green line in Fig. 6. In the 'MTS on' scenario, the chemistry of peroxy radicals in  
550 Semi II was reasonably described by introducing the source of complex alkoxy radicals,  
551 and the obs-to-mod ratio of peroxy radicals decreased from 2.2 to 1.3. Furthermore, the  
552 introduction of additional complex alkoxy radicals had minimal impact on HO<sub>x</sub>  
553 chemistry, with changes in daytime OH and HO<sub>2</sub> concentrations of less than  $5 \times 10^5$  cm<sup>-3</sup>  
554 and  $2.5 \times 10^7$  cm<sup>-3</sup>, respectively. This demonstrates the robustness of HO<sub>x</sub> radical in  
555 response to potential monoterpene.

556 Higher aldehyde chemistry is a concrete manifestation of verifying the  
557 aforementioned hypothesis for RO<sub>2</sub> sources (Yang et al., 2024b). The autoxidation process  
558 of R(CO)O<sub>2</sub>, encompasses a hydrogen migration process that transforms it into  
559 the ·OOR(CO)OOH radical (Wang et al., 2019b). This radical subsequently reacts with  
560 NO to yield the ·OR(CO)OOH radical. The ·OR(CO)OOH radical predominantly  
561 undergoes two successive rapid hydrogen migration reactions, ultimately resulting in the  
562 formation of HO<sub>2</sub> radicals and hydroperoxy carbonyl (HPC). Consequently, the HAM  
563 mechanism extends the lifetime of the RO<sub>2</sub> radical, providing a valuable complement to  
564 the unaccounted sources of RO<sub>2</sub> radicals. As depicted in Fig. 7, the incorporation of the  
565 HAM mechanism results in an approximate 7.4% and 12.5% increase in the  
566 concentrations of HO<sub>2</sub> and RO<sub>2</sub> radicals, respectively. It is important to note that the total  
567 concentrations of primary emitted aldehydes and the HPC group may be underestimated,  
568 which could lead to the aforementioned analysis being conservative in nature. Further  
569 exploration of the unaccounted sources of RO<sub>2</sub> radicals will be presented in Section 4.3.

570 **4.1.3 P(Ox) underestimation**

Upon completing the hypothetical investigation into the radical underestimation, a sensitivity comparison between observed and modeled P(O<sub>x</sub>) was conducted across the entire range of NO concentrations, as depicted in Fig. 8(a)(b). With increasing NO concentration, the overall P(O<sub>x</sub>) amplified, reaching a maximum of approximately 30 ppb/h. This variation has been validated through multiple observations in Wangdu, APHH, and other studies (Tan et al., 2017b; Whalley et al., 2021; Whalley et al., 2018). However, the imperfect understanding of the mechanisms related to peroxy radicals ultimately leads to misjudgment of the ozone production process in high NO regimes, with a degree of underestimation close to 10 times, as illustrated in Fig. 8(b).

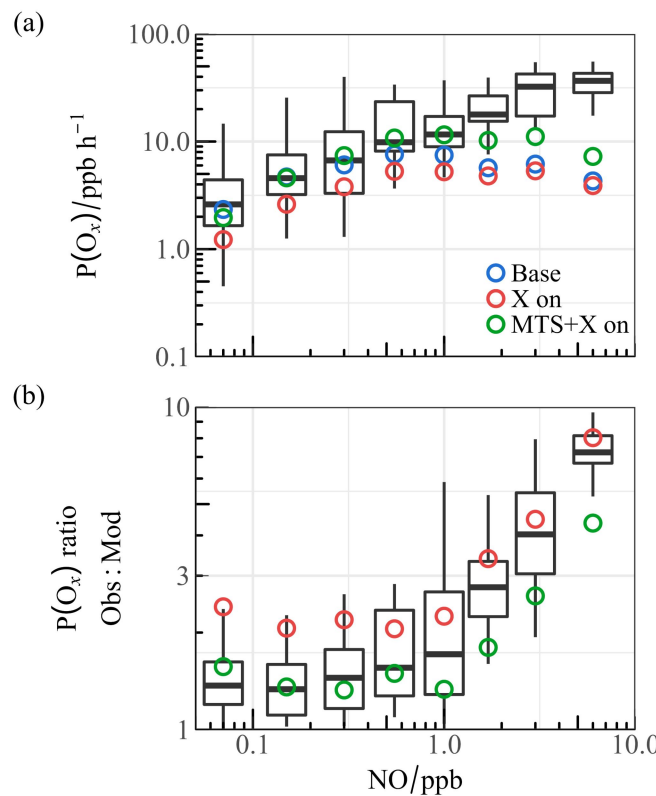


**Fig. 8.** The relationship between NO and (a) P(O<sub>x</sub>), (b) P(O<sub>x</sub>) (Obs:Mod). Boxplot diagrams are used to illustrate the minimum, 25th percentile, median, 75th percentile, and maximum values of the observed dataset. The circles represent the median values for the base model as well as for different mechanisms added to the model within various ranges.

Although the inclusion of the X mechanism improves the agreement between simulated and observed OH concentrations in the low-NO range, it has a negative effect on the P(O<sub>x</sub>) simulation. The introduction of a major source of RO<sub>2</sub> can help address the underestimation problem in the base scenario, as the lack of RO<sub>2</sub> species and related reaction rates is an important factor leading to deviations in the simulation of ozone

590 production rates (Tan et al., 2017a). The combination of the X mechanism and  
591 monoterpene chemistry is shown to better harmonize the relationship between HO<sub>2</sub> and  
592 RO<sub>2</sub>. Notably, the deficiency in the ozone generation mechanism was adequately  
593 explained within a certain range in the 'MTS+X On' scenario, leading to an enhancement  
594 in the simulation performance of P(O<sub>x</sub>) in the high NO<sub>x</sub> region (Fig. 8(b)). Therefore,  
595 reasonable simulation of the concentration of peroxy radicals is key to accurately  
596 quantifying the process of ozone generation.

## 597 **4.2 Effect of mechanism reconciliation on oxidation**

598 Both radical concentration and oxidation coordinating deficiency are worthy of  
599 examine (Fig. S9). To eliminate the influence of non-photolytic processes, only the  
600 daytime concentration range with  $j(O^1D)$  greater than  $5 \times 10^{-6} \text{ s}^{-1}$  was selected. The  
601 boxplots illustrate the ratio of observation to simulation (base model), with the circles  
602 representing the average values after integrating different mechanisms into the base  
603 scenario. In the low NO regime (NO < 1 ppb), the OH underestimation was consistently  
604 prominent as NO concentration decreased, and the base model was able to reasonably  
605 reflect the HO<sub>2</sub> distribution contrastly. As NO levels increased, the simulated OH  
606 concentration aligned well with the observation, but both HO<sub>2</sub> and RO<sub>2</sub> concentrations  
607 exhibited underprediction. RO<sub>2</sub> underestimation extended across the entire NO range, and  
608 could rise to over 10 times when NO levels reached about 10 ppb. Sensitivity tests based  
609 on the full suite of radical measurement revealed that the X mechanism accelerated OH  
610 regeneration, and the introduction of larger RO<sub>2</sub> alleviated the absence of certain sources  
611 by 2 to 4 times.

612 The coordinate ratios of radical serves as another test for RO<sub>x</sub> propagation (Fig. 9).  
613 The observed HO<sub>2</sub>/OH ratio is approximately 100, declining to some extent as the  
614 concentration of NO increases, which is consistent with previous studies (Griffith et al.,  
615 2016; Griffith et al., 2013). However, the base model does not accurately replicate the  
616 curve depicting the change in HO<sub>2</sub>/OH ratio, as shown in Fig. 9 (a). At low NO levels, the  
617 ratio significantly overestimated and shows a steeper decline compared to the base  
618 scenario as NO levels increase. Furthermore, the observed RO<sub>2</sub>/OH ratios remain around  
619 100, whereas the predicted values are significantly underestimated when NO exceeds 1  
620 ppb (refer to Fig. 9(b)). In terms of the observed HO<sub>2</sub>/RO<sub>2</sub> ratio, it maintains a relatively

constant trend within the range of 0.5 – 1.5, while the model overestimated by more than twice, highlighting an inconsistency between the conversion of  $\text{RO}_2 \rightarrow \text{HO}_2$ . The incorporation of the X mechanism has proven to be effective in a balanced  $\text{HO}_2/\text{OH}$  ratio as illustrated in Fig. 9(a), but amplifying the termination pathway for  $\text{HO}_2$  and  $\text{RO}_2$ , which altered the coordination between  $\text{RO}_2$  and OH across the entire NO range (Fig. 9(b)). The connection between unconditional OH source and larger  $\text{RO}_2$  isomerization in chemically complex environments is key to fully understanding tropospheric chemistry, and a better coordination of  $\text{HO}_2/\text{OH}$ ,  $\text{RO}_2/\text{OH}$ , and  $\text{HO}_2/\text{RO}_2$  ratios are established by incorporating additional mechanisms.

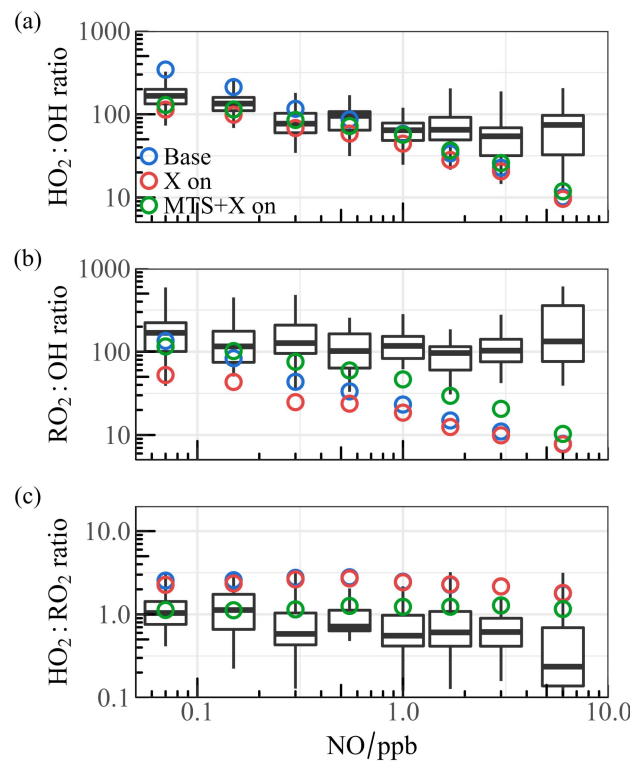
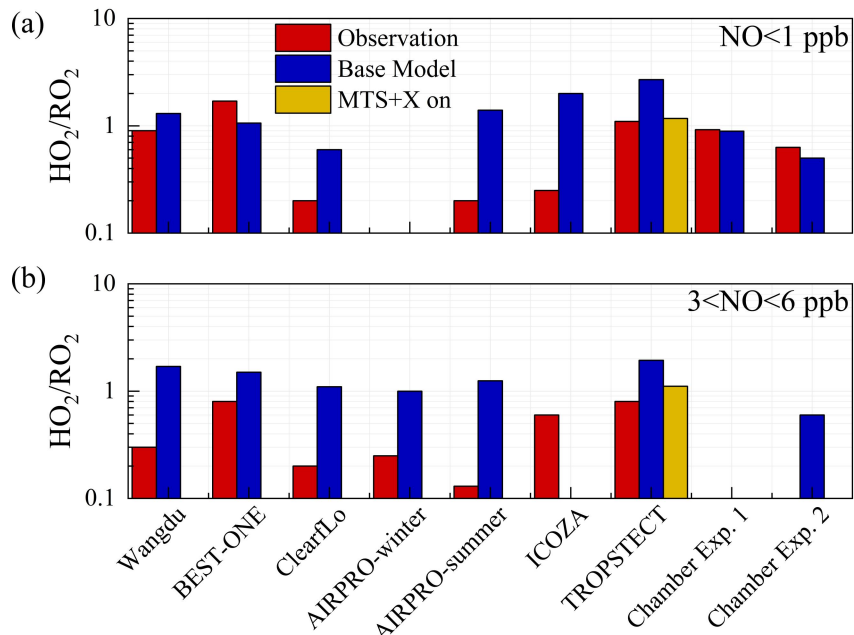


**Fig. 9.** The ratios for (a)  $\text{HO}_2/\text{OH}$ , (b)  $\text{RO}_2/\text{OH}$ , and (c)  $\text{HO}_2/\text{RO}_2$  show a correlation with NO levels. Boxplot diagrams are used to illustrate the minimum, 25th percentile, median, 75th percentile, and maximum values of the observed dataset. The circles represent the median values for the base model as well as for different mechanisms added to the model within various ranges.

The  $\text{HO}_2/\text{RO}_2$  parameter was utilized to explore the transformation relationship between  $\text{HO}_2$  and  $\text{RO}_2$  radicals. If  $\text{HO}_2$  is formed from an  $\text{RO}_2$  radical, it would result in an  $\text{HO}_2/\text{RO}_2$  radical concentration ratio of approximately 1. The  $\text{HO}_2/\text{RO}_2$  ratios derived from radical concentrations measured by laser-induced fluorescence instruments and calculated using the MCM or RACM models were summarized in Fig. 10. In field studies, the observed  $\text{HO}_2/\text{RO}_2$  ratios were between 0.2 - 1.7 under low-NO conditions ( $\text{NO} < 1$

641 ppb) and only 0.1 - 0.8 under high-NO conditions ( $3 < \text{NO} < 6$  ppb). From the  
 642 perspective of model-observation matching, except for three measurements in ClearfLo,  
 643 ICOZA and AIRPRO-summer campaigns, the  $\text{HO}_2/\text{RO}_2$  ratios in other regions could be  
 644 reasonably reflected by the MCM or RACM2 mechanisms(Woodward-Massey et al.,  
 645 2023; Whalley et al., 2021; Whalley et al., 2018; Färber et al., 2024). However, the ratio  
 646 is generally underestimated under high NO conditions, reaching up to 5 times in ClearfLo.  
 647 According to the latest chamber experiments, the  $\text{HO}_2/\text{RO}_2$  radical concentration ratios  
 648 for VOCs forming  $\text{HO}_2$  are 0.6 for both one-step and two-step reactions. Therefore, the  
 649 extremely low  $\text{HO}_2/\text{RO}_2$  ratios observed in field campaigns can only be explained if  
 650 almost all  $\text{RO}_2$  radicals undergo multiple-step reactions before forming  $\text{HO}_2$ . During the  
 651 TROPSTECT campaign, the observed  $\text{HO}_2/\text{RO}_2$  remains at 1.1 and 0.8 under low-NO  
 652 and high-NO conditions, respectively. After considering the complex sources of complex  
 653 alkoxy radicals in the 'MTS+X' scenario, the simulated values of  $\text{HO}_2/\text{RO}_2$  in both  
 654 low-NO and high-NO regions match the observed values well.



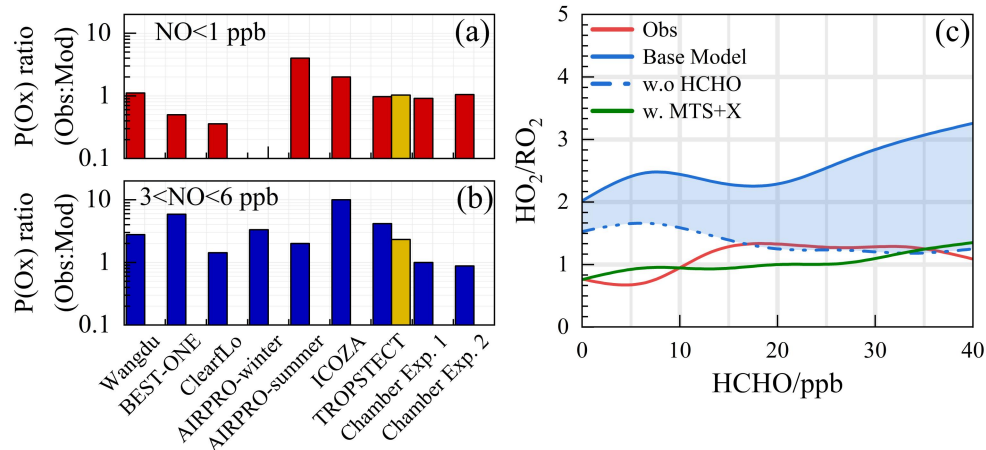
655

656 **Fig. 10.** Summary of the  $\text{HO}_2/\text{RO}_2$  ratios derived from radical concentrations measured by laser-induced fluorescence  
 657 instruments and calculated using the MCM or RACM models under (a) low-NO and (b) high-NO conditions.  
 658 Charmber Exp. 1 and Charmber Exp. 2 denotes the parameters by single-step  $\text{HO}_2$  formation and multi-step  $\text{HO}_2$   
 659 formation determined in the chamber by (Färber et al., 2024).

#### 660 4.3 Missing OVOCs sources influence ozone production

661 The consistency between model predictions and observed measurements for ozone

662 production, akin to the concentration ratio of  $\text{HO}_2/\text{RO}_2$ , is depicted in Fig. 11(a)(b). In  
 663 areas with low NO levels, the ratio of modeled to actual ozone production ranges from  
 664 0.5 to 2, with the exception of the ClearfLo and AIRPRO-summer  
 665 datasets(Woodward-Massey et al., 2023; Whalley et al., 2021). Conversely, under high  
 666 NO conditions (with NO concentrations between 3 and 6 ppbv), the ozone production  
 667 rate ( $\text{P}(\text{Ox})$ ) derived from measured radical concentrations typically exceeds that of the  
 668 base model's predictions by more than threefold. Laboratory experiments focusing on the  
 669 oxidation of representative VOCs suggest that ozone production can be enhanced by  
 670 approximately 25% for the anthropogenic VOCs under investigation(Färber et al., 2024).  
 671 The MTS+X scenario represents an effort to enhance the congruence between modeled  
 672 and measured radical concentrations. The incorporation of OVOCs and larger alkoxy  
 673 radicals derived from monoterpenes has refined the model-measurement agreement for  
 674 ozone formation under high NO conditions, reducing the discrepancy from 4.17 to 2.33.  
 675 This substantiates the hypothesis of sensitivity analysis concerning ozone generation, as  
 676 detailed in Section 4.2 and illustrated in Fig. S10.



677

678 **Fig. 11.** Summary of the  $\text{P}(\text{Ox})_{\text{Obs}}/\text{P}(\text{Ox})_{\text{Mod}}$  under **(a)** low-NO and **(b)** high-NO conditions.**(c)** The ratios for  
 679  $\text{HO}_2/\text{RO}_2$  show a correlation with HCHO levels. The blue shading represents the range of variation from constrained to  
 680 unconstrained formaldehyde conditions. Chamber Exp. 1 and Chamber Exp. 2 denotes the parameters by single-step  
 681 HO<sub>2</sub> formation and multi-step HO<sub>2</sub> formation determined in the chamber by (Färber et al., 2024).

682 The reasons for the discrepancy between simulated and observed values for ozone  
 683 production deserve further investigation. As depicted in Fig.11(c), the simulated  
 684 HO<sub>2</sub>/RO<sub>2</sub> ratios display a robust positive correlation with photochemical activity,  
 685 fluctuating between 2 and 4. A notable feature during severe ozone pollution is the  
 686 intense distribution of formaldehyde, with an average concentration of  $21.81 \pm 4.57$  ppb

687 (11:00 – 13:00). While formaldehyde acts as a precursor for  $\text{HO}_2$  radicals, it does not  
688 directly generate  $\text{RO}_2$  radicals. The contributions of OVOCs to the ROx radical do not  
689 exhibit the same intensity as formaldehyde, and the current mechanism encounters  
690 difficulties in replicating formaldehyde concentrations (Fig. S11). The simulation of  
691 formaldehyde concentrations using the MCM v3.3.1 mechanism has shown improvement,  
692 indicating that the secondary formation of unmeasured species, such as OVOCs, will  
693 feedback on  $\text{RO}_2$  radical levels. When formaldehyde levels are unconstrained, the  
694 simulated  $\text{HO}_2/\text{RO}_2$  ratios align with observations, suggesting that under the prevailing  
695 chemical mechanism, the photochemical efficiency of formaldehyde and other OVOCs is  
696 similar. Therefore, an empirical hypothesis is proposed to amplify the concentration of  
697 higher-order aldehydes by a factor of about 4, which is the proportion of formaldehyde  
698 concentration underestimated by the model. The qualitative assessment of the impact of  
699 missing aldehyde primary emissions on  $\text{RO}_2$  radical concentrations was combined with  
700 the HAM mechanism across the entire photochemical spectrum (Fig.S12). Enhanced  
701 impact of aldehyde autoxidation in the presence of weak photochemical conditions could  
702 alter the simulated levels of OH and  $\text{HO}_2$  radicals by approximately 13.9% and 18.1%,  
703 respectively. However, higher ALD concentrations will be achieved under intensive  
704 photochemical conditions, leading to the gradual dominance of the sink channels for OH  
705 + OVOCs, with the effect of autoxidation mechanisms gradually decreasing.  $\text{RO}_2$  radical  
706 concentrations is notably more sensitive to the HAM mechanism, where incorporates  
707 additional OVOCs, can enhance the simulation of  $\text{RO}_2$  radical concentrations by 20 -  
708 40%. Consequently, although limiting formaldehyde can partially offset the  $\text{HO}_2$  radical  
709 cycle and enhance the precision of HOx radical chemistry studies, additional  
710 measurements should be undertaken for other OVOCs, coupled with the deployment of  
711 full-chain radical detection systems, to accurately elucidate the oxidation processes under  
712 severe ozone pollution conditions.

## 713 5 Conclusion

714 The full suite radical measurement of OH,  $\text{HO}_2$ ,  $\text{RO}_2$  and  $k_{\text{OH}}$  was first deployed in  
715 the YRD region (TROPSTECT) and encountered with a prolonged ozone pollution in  
716 September 2020. The diurnal peaks of radicals exhibited considerable variation due to

717 environmental factors, showing ranges of  $3.6$  to  $27.1 \times 10^6 \text{ cm}^{-3}$  for OH,  $2.1$  to  $33.2 \times 10^8 \text{ cm}^{-3}$  for HO<sub>2</sub>, and  $4.9$  to  $30.5 \times 10^8 \text{ cm}^{-3}$  for RO<sub>2</sub>. Continuous  $k_{\text{OH}}$  data fell within a range  
718 of  $8.6$  –  $30.2 \text{ s}^{-1}$ , demonstrating the dominant behavior of organic species in diurnal  
719 reactivity. Furthermore, observations in the YRD region were found to be similar to those  
720 in other megacities, suggesting no significant regional differences in oxidation levels  
721 were observed in agglomerations overall.

723 At a heavy ozone pollution episode, the oxidation level reached intensive compared  
724 with other sites, and the simulated OH, HO<sub>2</sub>, and RO<sub>2</sub> radicals provided by the  
725 RACM2-LIM1 mechanism failed to adequately match the observed data both in radical  
726 concentration and experimental radical budget. Sensitivity tests based on the full suite of  
727 radical measurement revealed that the X mechanism accelerated OH regeneration, and  
728 the introduction of larger alkoxy radicals alleviated the RO<sub>2</sub>-related imbalance. The HAM  
729 mechanism effectively complements the non-traditional regeneration of OH radicals,  
730 improving by  $4.4\%$  -  $6.0\%$  compared to the base scenario, while the concentrations of  
731 HO<sub>2</sub> and RO<sub>2</sub> radicals increased by approximately  $7.4\%$  and  $12.5\%$ , respectively. The  
732 incorporation of complex processes enabled better coordination of HO<sub>2</sub>/OH, RO<sub>2</sub>/OH,  
733 and HO<sub>2</sub>/RO<sub>2</sub> ratios, and adequately addressed the deficiency in the ozone generation  
734 mechanism within a certain range. Incorporation of OVOCs and larger alkoxy radicals  
735 derived from monoterpenes improved the measurement-model consistency for ozone  
736 formation under high NO conditions, reducing the discrepancy from  $4.17$  to  $2.33$ , which  
737 corroborates the hypothesis of sensitivity analysis in the context of ozone generation.  
738 This study enabled a deeper understanding of the tropospheric radical chemistry at play.  
739 Notably,

740 ✓ A full suite of radical measurement can untangle the gap-bridge for the base model in  
741 more chemically-complex environments as an hypothesis of sensitivity tests.  
742 ✓ Additional measurements targeting more OVOCs should also be conducted to fulfill  
743 the RO<sub>2</sub>-related imbalance, and then accurately elucidating the oxidation under  
744 severe ozone pollution.

745

746 **Financial support**

747 This work was supported by the National Key R&D Program of China  
748 (2022YFC3700301), the National Natural Science Foundation of China (62275250,  
749 U19A2044, 42030609), the Natural Science Foundation of Anhui Province (No.  
750 2008085J20), the Anhui Provincial Key R&D Program (2022l07020022), and the  
751 Distinguished Program of Jianghuai Talents Program of Excellence (HYRCSTZ202401).

752 **Data availability**

753 The data used in this study are available upon request (rzhu@aiofm.ac.cn).

754 **Author contributions**

755 WQ Liu, PH Xie, RZ Hu contributed to the conception of this study. RZ Hu and GX  
756 Zhang performed the data analyses and manuscript writing. All authors contributed to  
757 measurements, discussed results, and commented on the paper.

758 **Competing interests**

759 The contact author has declared that none of the authors has any competing interests.  
760

## 761 References

762 Duan, J., Qin, M., Ouyang, B., Fang, W., Li, X., Lu, K., Tang, K., Liang, S., Meng, F., Hu, Z., Xie, P., Liu,  
763 W., and Häsler, R.: Development of an incoherent broadband cavity-enhanced absorption spectrometer for  
764 in situ measurements of HONO and NO<sub>2</sub>, *Atmos Meas Tech*, 11, 4531-4543, 10.5194/amt-11-4531-2018,  
765 2018.

766 Färber, M., Fuchs, H., Bohn, B., Carlsson, P. T. M., Gkatzelis, G. I., Marcillo Lara, A. C., Rohrer, F.,  
767 Vereecken, L., Wedel, S., Wahner, A., and Novelli, A.: Effect of the Alkoxy Radical Chemistry on the  
768 Ozone Formation from Anthropogenic Organic Compounds Investigated in Chamber Experiments, *ACS*  
769 *ES&T Air*, 1, 1096-1111, 10.1021/acsestair.4c00064, 2024.

770 Fuchs, H., Holland, F., and Hofzumahaus, A.: Measurement of tropospheric RO<sub>2</sub> and HO<sub>2</sub> radicals by a  
771 laser-induced fluorescence instrument, *Rev of Sci Inst*, 79, 084104, 10.1063/1.2968712, 2008.

772 George, L. A., Hard, T. M., and O'Brien, R. J.: Measurement of free radicals OH and HO<sub>2</sub> in Los Angeles  
773 smog, *J Geophys Res-Atmos*, 104, 11643-11655, 1999.

774 Griffith, S. M., Hansen, R. F., Dusanter, S., Stevens, P. S., Alaghmand, M., Bertman, S. B., Carroll, M. A.,  
775 Erickson, M., Galloway, M., Grossberg, N., Hottle, J., Hou, J., Jobson, B. T., Kamprath, A., Keutsch, F. N.,  
776 Lefer, B. L., Mielke, L. H., O'Brien, A., Shepson, P. B., Thurlow, M., Wallace, W., Zhang, N., and Zhou, X.  
777 L.: OH and HO<sub>2</sub> radical chemistry during PROPHET 2008 and CABINEX 2009-Part 1: Measurements and  
778 model comparison, *Atmos Chem Phys*, 13, 5403-5423, 10.5194/acp-13-5403-2013, 2013.

779 Griffith, S. M., Hansen, R. F., Dusanter, S., Michoud, V., Gilman, J. B., Kuster, W. C., Veres, P. R., Graus,  
780 M., de Gouw, J. A., Roberts, J., Young, C., Washenfelder, R., Brown, S. S., Thalman, R., Waxman, E.,  
781 Volkamer, R., Tsai, C., Stutz, J., Flynn, J. H., Grossberg, N., Lefer, B., Alvarez, S. L., Rappenglueck, B.,  
782 Mielke, L. H., Osthoff, H. D., and Stevens, P. S.: Measurements of hydroxyl and hydroperoxy radicals  
783 during CalNex-LA: Model comparisons and radical budgets, *J Geophys Res-Atmos*, 121, 4211-4232,  
784 10.1002/2015jd024358, 2016.

785 Heard, D. E. and Pilling, M. J.: Measurement of OH and HO<sub>2</sub> in the troposphere, *Chemical reviews*, 103,  
786 5163-5198, 10.1021/cr020522s, 2003.

787 Hofzumahaus, A., Rohrer, F., Lu, K., Bohn, B., Brauers, T., Chang, C.-C., Fuchs, H., Holland, F., Kita, K.,  
788 Kondo, Y., Li, X., Lou, S., Shao, M., Zeng, L., Wahner, A., and Zhang, Y.: Amplified Trace Gas Removal in  
789 the Troposphere, *Science*, 324, 1702-1704, 10.1126/science.1164566, 2009.

790 Hu, B., Duan, J., Hong, Y., Xu, L., Li, M., Bian, Y., Qin, M., Fang, W., Xie, P., and Chen, J.: Exploration of  
791 the atmospheric chemistry of nitrous acid in a coastal city of southeastern China: results from  
792 measurements across four seasons, *Atmos Chem Phys*, 22, 371-393, 10.5194/acp-22-371-2022, 2022.

793 Huang, J., Pan, X., Guo, X., and Li, G.: Health impact of China's Air Pollution Prevention and Control  
794 Action Plan: an analysis of national air quality monitoring and mortality data, *Lancet Planet Health*, 2,  
795 e313-e323, 10.1016/S2542-5196(18)30141-4, 2018.

796 Huang, X., Ding, A., Wang, Z., Ding, K., Gao, J., Chai, F., and Fu, C.: Amplified transboundary transport  
797 of haze by aerosol-boundary layer interaction in China, *Nature Geoscience*, 13, 428-434,  
798 10.1038/s41561-020-0583-4, 2020.

799 Jenkin, M. E., Saunders, S. M., and Pilling, M. J.: The tropospheric degradation of volatile organic  
800 compounds: A protocol for mechanism development, *Atmos Environ*, 31, 81-104,  
801 10.1016/s1352-2310(96)00105-7, 1997.

802 Jenkin, M. E., Saunders, S. M., Wagner, V., and Pilling, M. J.: Protocol for the development of the Master  
803 Chemical Mechanism, MCM v3 (Part B): tropospheric degradation of aromatic volatile organic compounds,  
804 *Atmos Chem Phys*, 3, 181-193, 10.5194/acp-3-181-2003, 2003.

805 Jia, W., Zhang, X., and Wang, Y.: Assessing the pollutant evolution mechanisms of heavy pollution  
806 episodes in the Yangtze-Huaihe valley: A multiscale perspective, *Atmos Environ*, 244,  
807 10.1016/j.atmosenv.2020.117986, 2021.

808 Kanaya, Y., Hofzumahaus, A., Dorn, H. P., Brauers, T., Fuchs, H., Holland, F., Rohrer, F., Bohn, B.,  
809 Tillmann, R., Wegener, R., Wahner, A., Kajii, Y., Miyamoto, K., Nishida, S., Watanabe, K., Yoshino, A.,  
810 Kubistin, D., Martinez, M., Rudolf, M., Harder, H., Berresheim, H., Elste, T., Plass-Duelmer, C., Stange, G.,  
811 Kleffmann, J., Elshorbany, Y., and Schurath, U.: Comparisons of observed and modeled OH and HO<sub>2</sub>  
812 concentrations during the ambient measurement period of the HO(x)Comp field campaign, *Atmos Chem  
813 Phys*, 12, 2567-2585, 10.5194/acp-12-2567-2012, 2012.

814 Levy, H.: Normal Atmosphere: Large Radical and Formaldehyde Concentrations Predicted, *Science*, 173,

815 141-143, 10.1126/science.173.3992.141, 1971.  
 816 Li, S., Lu, K., Ma, X., Yang, X., Chen, S., and Zhang, Y.: Field measurement of the organic peroxy radicals  
 817 by the low-pressure reactor plus laser-induced fluorescence spectroscopy, Chinese Chemical Letters, 31,  
 818 2799-2802, 10.1016/j.cclet.2020.07.051, 2020.  
 819 Liu, S., Li, X., Shen, X., Zeng, L., Huang, X., Zhu, B., Lin, L., and Lou, S.: Measurement and partition  
 820 analysis of atmospheric OH reactivity in autumn in Shenzhen, *Acta Scientiae Circumstantiae*, 39,  
 821 3600-3610, 2019.  
 822 Liu, Y., Li, J., Ma, Y., Zhou, M., Tan, Z., Zeng, L., Lu, K., and Zhang, Y.: A review of gas-phase chemical  
 823 mechanisms commonly used in atmospheric chemistry modelling, *Journal of Environmental Sciences*,  
 824 10.1016/j.jes.2022.10.031, 2022.  
 825 Liu, Z., Wang, Y., Hu, B., Lu, K., Tang, G., Ji, D., Yang, X., Gao, W., Xie, Y., Liu, J., Yao, D., Yang, Y., and  
 826 Zhang, Y.: Elucidating the quantitative characterization of atmospheric oxidation capacity in Beijing, China,  
 827 *Sci Total Environ*, 771, 10.1016/j.scitotenv.2021.145306, 2021.  
 828 Lou, S., Holland, F., Rohrer, F., Lu, K., Bohn, B., Brauers, T., Chang, C. C., Fuchs, H., Haseler, R., Kita, K.,  
 829 Kondo, Y., Li, X., Shao, M., Zeng, L., Wahner, A., Zhang, Y., Wang, W., and Hofzumahaus, A.:  
 830 Atmospheric OH reactivities in the Pearl River Delta – China in summer 2006: measurement and model  
 831 results, *Atmos Chem Phys*, 10, 11243–11260, 10.5194/acp-10-11243-2010, 2010.  
 832 Lu, K., Guo, S., Tan, Z., Wang, H., Shang, D., Liu, Y., Li, X., Wu, Z., Hu, M., and Zhang, Y.: Exploring  
 833 atmospheric free-radical chemistry in China: the self-cleansing capacity and the formation of secondary air  
 834 pollution, *Natl. Sci. Rev.*, 6, 579-594, 10.1093/nsr/nwy073, 2019a.  
 835 Lu, K. D., Guo, S., Tan, Z. F., Wang, H. C., Shang, D. J., Liu, Y. H., Li, X., Wu, Z. J., Hu, M., and Zhang, Y.  
 836 H.: Exploring atmospheric free-radical chemistry in China: the self-cleansing capacity and the formation of  
 837 secondary air pollution, *Natl. Sci. Rev.*, 6, 579-594, 10.1093/nsr/nwy073, 2019b.  
 838 Lu, K. D., Rohrer, F., Holland, F., Fuchs, H., Bohn, B., Brauers, T., Chang, C. C., Haeseler, R., Hu, M., Kita,  
 839 K., Kondo, Y., Li, X., Lou, S. R., Nehr, S., Shao, M., Zeng, L. M., Wahner, A., Zhang, Y. H., and  
 840 Hofzumahaus, A.: Observation and modelling of OH and HO<sub>2</sub> concentrations in the Pearl River Delta 2006:  
 841 a missing OH source in a VOC rich atmosphere, *Atmos Chem Phys*, 12, 1541-1569,  
 842 10.5194/acp-12-1541-2012, 2012.  
 843 Ma, X., Tan, Z., Lu, K., Yang, X., Chen, X., Wang, H., Chen, S., Fang, X., Li, S., Li, X., Liu, J., Liu, Y.,  
 844 Lou, S., Qiu, W., Wang, H., Zeng, L., and Zhang, Y.: OH and HO<sub>2</sub> radical chemistry at a suburban site  
 845 during the EXPLORE-YRD campaign in 2018, *Atmos Chem Phys*, 22, 7005-7028,  
 846 10.5194/acp-22-7005-2022, 2022.  
 847 Ma, X. F., Tan, Z. F., Lu, K. D., Yang, X. P., Liu, Y. H., Li, S. L., Li, X., Chen, S. Y., Novelli, A., Cho, C.  
 848 M., Zeng, L. M., Wahner, A., and Zhang, Y. H.: Winter photochemistry in Beijing: Observation and model  
 849 simulation of OH and HO<sub>2</sub> radicals at an urban site, *Sci Total Environ*, 685, 85-95,  
 850 10.1016/j.scitotenv.2019.05.329, 2019.  
 851 Mao, J., Ren, X., Chen, S., Brune, W. H., Chen, Z., Martinez, M., Harder, H., Lefer, B., Rappenglück, B.,  
 852 Flynn, J., and Leuchner, M.: Atmospheric oxidation capacity in the summer of Houston 2006: Comparison  
 853 with summer measurements in other metropolitan studies, *Atmos Environ*, 44, 4107-4115,  
 854 10.1016/j.atmosenv.2009.01.013, 2010.  
 855 Martinez, M., Harder, H., Kovacs, T. A., Simpas, J. B., Bassis, J., Lesher, R., Brune, W. H., Frost, G. J.,  
 856 Williams, E. J., Stroud, C. A., Jobson, B. T., Roberts, J. M., Hall, S. R., Shetter, R. E., Wert, B., Fried, A.,  
 857 Alicke, B., Stutz, J., Young, V. L., White, A. B., and Zamora, R. J.: OH and HO<sub>2</sub> concentrations, sources,  
 858 and loss rates during the Southern Oxidants Study in Nashville, Tennessee, summer 1999, *J Geophys  
 859 Res-Atmos*, 108, 10.1029/2003jd003551, 2003.  
 860 Peeters, J., Muller, J. F., Stavrakou, T., and Nguyen, V. S.: Hydroxyl Radical Recycling in Isoprene  
 861 Oxidation Driven by Hydrogen Bonding and Hydrogen Tunneling: The Upgraded LIM1 Mechanism, *J  
 862 Phys Chem A*, 118, 8625-8643, 10.1021/jp5033146, 2014.  
 863 Qu, H., Wang, Y., Zhang, R., Liu, X., Huey, L. G., Sjostedt, S., Zeng, L., Lu, K., Wu, Y., Shao, M., Hu, M.,  
 864 Tan, Z., Fuchs, H., Broch, S., Wahner, A., Zhu, T., and Zhang, Y.: Chemical Production of Oxygenated  
 865 Volatile Organic Compounds Strongly Enhances Boundary-Layer Oxidation Chemistry and Ozone  
 866 Production, *Environ Sci Technol*, 10.1021/acs.est.1c04489, 2021.  
 867 Ren, X., Olson, J. R., Crawford, J. H., Brune, W. H., Mao, J., Long, R. B., Chen, Z., Chen, G., Avery, M. A.,  
 868 Sachse, G. W., Barrick, J. D., Diskin, G. S., Huey, L. G., Fried, A., Cohen, R. C., Heikes, B., Wennberg, P.  
 869 O., Singh, H. B., Blake, D. R., and Shetter, R. E.: HO<sub>x</sub> chemistry during INTEX-A 2004: Observation,  
 870 model calculation, and comparison with previous studies, *J Geophys Res-Atmos*, 113,

871 10.1029/2007jd009166, 2008.

872 Rohrer, F., Lu, K., Hofzumahaus, A., Bohn, B., Brauers, T., Chang, C.-C., Fuchs, H., Haeseler, R., Holland,  
873 F., Hu, M., Kita, K., Kondo, Y., Li, X., Lou, S., Oebel, A., Shao, M., Zeng, L., Zhu, T., Zhang, Y., and  
874 Wahner, A.: Maximum efficiency in the hydroxyl-radical-based self-cleansing of the troposphere, *Nature  
875 Geoscience*, 7, 559-563, 10.1038/ngeo2199, 2014.

876 Shi, X., Ge, Y., Zheng, J., Ma, Y., Ren, X., and Zhang, Y.: Budget of nitrous acid and its impacts on  
877 atmospheric oxidative capacity at an urban site in the central Yangtze River Delta region of China, *Atmos  
878 Environ*, 238, 10.1016/j.atmosenv.2020.117725, 2020.

879 Slater, E. J., Whalley, L. K., Woodward-Massey, R., Ye, C., Lee, J. D., Squires, F., Hopkins, J. R., Dunmore,  
880 R. E., Shaw, M., Hamilton, J. F., Lewis, A. C., Crilley, L. R., Kramer, L., Bloss, W., Vu, T., Sun, Y., Xu, W.,  
881 Yue, S., Ren, L., Acton, W. J. F., Hewitt, C. N., Wang, X., Fu, P., and Heard, D. E.: Elevated levels of OH  
882 observed in haze events during wintertime in central Beijing, *Atmos Chem Phys*, 20, 14847-14871,  
883 10.5194/acp-20-14847-2020, 2020.

884 Song, H., Lu, K., Dong, H., Tan, Z., Chen, S., Zeng, L., and Zhang, Y.: Reduced Aerosol Uptake of  
885 Hydroperoxyl Radical May Increase the Sensitivity of Ozone Production to Volatile Organic Compounds,  
886 *Environmental Science & Technology Letters*, 9, 22-29, 10.1021/acs.estlett.1c00893, 2021.

887 Stockwell, W. R., Kirchner, F., Kuhn, M., and Seefeld, S.: A new mechanism for regional atmospheric  
888 chemistry modeling, *J Geophys Res-Atmos*, 102, 25847-25879, 10.1029/97jd00849, 1997.

889 Stone, D., Whalley, L. K., and Heard, D. E.: Tropospheric OH and HO<sub>2</sub> radicals: field measurements and  
890 model comparisons, *Chemical Society reviews*, 41, 6348-6404, 10.1039/c2cs35140d, 2012.

891 Tan, Z., Ma, X., Lu, K., Jiang, M., Zou, Q., Wang, H., Zeng, L., and Zhang, Y.: Direct evidence of local  
892 photochemical production driven ozone episode in Beijing: A case study, *Sci Total Environ*, 800, 148868,  
893 10.1016/j.scitotenv.2021.148868, 2021.

894 Tan, Z., Lu, K., Jiang, M., Su, R., Wang, H., Lou, S., Fu, Q., Zhai, C., Tan, Q., Yue, D., Chen, D., Wang, Z.,  
895 Xie, S., Zeng, L., and Zhang, Y.: Daytime atmospheric oxidation capacity in four Chinese megacities  
896 during the photochemically polluted season: a case study based on box model simulation, *Atmos Chem  
897 Phys*, 19, 3493-3513, 10.5194/acp-19-3493-2019, 2019a.

898 Tan, Z., Fuchs, H., Lu, K., Hofzumahaus, A., Bohn, B., Broch, S., Dong, H., Gomm, S., Haeseler, R., He,  
899 L., Holland, F., Li, X., Liu, Y., Lu, S., Rohrer, F., Shao, M., Wang, B., Wang, M., Wu, Y., Zeng, L., Zhang,  
900 Y., Wahner, A., and Zhang, Y.: Radical chemistry at a rural site (Wangdu) in the North China Plain:  
901 observation and model calculations of OH, HO<sub>2</sub> and RO<sub>2</sub> radicals, *Atmos Chem Phys*, 17, 663-690,  
902 10.5194/acp-17-663-2017, 2017a.

903 Tan, Z. F., Lu, K. D., Dong, H. B., Hu, M., Li, X., Liu, Y. H., Lu, S. H., Shao, M., Su, R., Wang, H. C., Wu,  
904 Y. S., Wahner, A., and Zhang, Y. H.: Explicit diagnosis of the local ozone production rate and the  
905 ozone-NO<sub>x</sub>-VOC sensitivities, *Sci. Bull.*, 63, 1067-1076, 10.1016/j.scib.2018.07.001, 2018.

906 Tan, Z. F., Lu, K. D., Hofzumahaus, A., Fuchs, H., Bohn, B., Holland, F., Liu, Y. H., Rohrer, F., Shao, M.,  
907 Sun, K., Wu, Y. S., Zeng, L. M., Zhang, Y. S., Zou, Q., Kiendler-Scharr, A., Wahner, A., and Zhang, Y. H.:  
908 Experimental budgets of OH, HO<sub>2</sub>, and RO<sub>2</sub> radicals and implications for ozone formation in the Pearl  
909 River Delta in China 2014, *Atmos Chem Phys*, 19, 7129-7150, 10.5194/acp-19-7129-2019, 2019b.

910 Tan, Z. F., Fuchs, H., Lu, K. D., Hofzumahaus, A., Bohn, B., Broch, S., Dong, H. B., Gomm, S., Haseler, R.,  
911 He, L. Y., Holland, F., Li, X., Liu, Y., Lu, S. H., Rohrer, F., Shao, M., Wang, B. L., Wang, M., Wu, Y. S.,  
912 Zeng, L. M., Zhang, Y. S., Wahner, A., and Zhang, Y. H.: Radical chemistry at a rural site (Wangdu) in the  
913 North China Plain: observation and model calculations of OH, HO<sub>2</sub> and RO<sub>2</sub> radicals, *Atmos Chem Phys*,  
914 17, 663-690, 10.5194/acp-17-663-2017, 2017b.

915 Wang, F., Hu, R., Xie, P., Wang, Y., Chen, H., Zhang, G., and Liu, W.: Calibration source for OH radical  
916 based on synchronous photolysis, *Acta Phys Sin-Ch Ed*, 69, 2020.

917 Wang, F. Y., Hu, R. Z., Chen, H., Xie, P. H., Wang, Y. H., Li, Z. Y., Jin, H. W., Liu, J. G., and Liu, W. Q.:  
918 Development of a field system for measurement of tropospheric OH radical using laser-induced  
919 fluorescence technique, *Opt. Express*, 27, A419-A435, 10.1364/oe.27.00a419, 2019a.

920 Wang, H., Lu, K., Tan, Z., Chen, X., Liu, Y., and Zhang, Y.: Formation mechanism and control strategy for  
921 particulate nitrate in China, *Journal of Environmental Sciences*, 10.1016/j.jes.2022.09.019, 2022a.

922 Wang, H., Ma, X., Tan, Z., Wang, H., Chen, X., Chen, S., Gao, Y., Liu, Y., Liu, Y., Yang, X., Yuan, B., Zeng,  
923 L., Huang, C., Lu, K., and Zhang, Y.: Anthropogenic monoterpenes aggravating ozone pollution, *Natl. Sci.  
924 Rev.*, 9, 2022b.

925 Wang, S.-n., Wu, R.-r., and Wang, L.-m.: Role of hydrogen migrations in carbonyl peroxy radicals in the  
926 atmosphere, *Chinese J Chem Phys*, 32, 457-466, 10.1063/1674-0068/cjcp1811265, 2019b.

927 Wang, T., Xue, L., Feng, Z., Dai, J., Zhang, Y., and Tan, Y.: Ground-level ozone pollution in China: a  
928 synthesis of recent findings on influencing factors and impacts, *Environmental Research Letters*,  
929 10.1088/1748-9326/ac69fe, 2022c.

930 Wang, W., Yuan, B., Su, H., Cheng, Y., Qi, J., Wang, S., Song, W., Wang, X., Xue, C., Ma, C., Bao, F.,  
931 Wang, H., Lou, S., and Shao, M.: A large role of missing volatile organic compound reactivity from  
932 anthropogenic emissions in ozone pollution regulation, *Atmos Chem Phys*, 24, 4017-4027,  
933 10.5194/acp-24-4017-2024, 2024.

934 Wang, W., Yuan, B., Peng, Y., Su, H., Cheng, Y., Yang, S., Wu, C., Qi, J., Bao, F., Huangfu, Y., Wang, C.,  
935 Ye, C., Wang, Z., Wang, B., Wang, X., Song, W., Hu, W., Cheng, P., Zhu, M., Zheng, J., and Shao, M.:  
936 Direct observations indicate photodegradable oxygenated volatile organic compounds (OVOCs) as larger  
937 contributors to radicals and ozone production in the atmosphere, *Atmos Chem Phys*, 22, 4117-4128,  
938 10.5194/acp-22-4117-2022, 2022d.

939 Wang, Y., Hu, R., Xie, P., Chen, H., Wang, F., Liu, X., Liu, J., and Liu, W.: Measurement of tropospheric  
940 HO<sub>2</sub> radical using fluorescence assay by gas expansion with low interferences, *J Environ Sci (China)*, 99,  
941 40-50, 10.1016/j.jes.2020.06.010, 2021.

942 Whalley, L. K., Blitz, M. A., Desservettaz, M., Seakins, P. W., and Heard, D. E.: Reporting the sensitivity  
943 of laser-induced fluorescence instruments used for HO<sub>2</sub> detection to an interference from RO<sub>2</sub> radicals and  
944 introducing a novel approach that enables HO<sub>2</sub> and certain RO<sub>2</sub> types to be selectively measured, *Atmos  
945 Meas Tech*, 6, 3425-3440, 10.5194/amt-6-3425-2013, 2013.

946 Whalley, L. K., Stone, D., Dunmore, R., Hamilton, J., Hopkins, J. R., Lee, J. D., Lewis, A. C., Williams, P.,  
947 Kleffmann, J., Laufs, S., Woodward-Massey, R., and Heard, D. E.: Understanding in situ ozone production  
948 in the summertime through radical observations and modelling studies during the Clean air for London  
949 project (ClearfLo), *Atmos Chem Phys*, 18, 2547-2571, 10.5194/acp-18-2547-2018, 2018.

950 Whalley, L. K., Slater, E. J., Woodward-Massey, R., Ye, C., Lee, J. D., Squires, F., Hopkins, J. R., Dunmore,  
951 R. E., Shaw, M., Hamilton, J. F., Lewis, A. C., Mehra, A., Worrall, S. D., Bacak, A., Bannan, T. J., Coe, H.,  
952 Percival, C. J., Ouyang, B., Jones, R. L., Crilley, L. R., Kramer, L. J., Bloss, W. J., Vu, T., Kotthaus, S.,  
953 Grimmond, S., Sun, Y., Xu, W., Yue, S., Ren, L., Acton, W. J. F., Hewitt, C. N., Wang, X., Fu, P., and Heard,  
954 D. E.: Evaluating the sensitivity of radical chemistry and ozone formation to ambient VOCs and NO<sub>x</sub> in  
955 Beijing, *Atmos Chem Phys*, 21, 2125-2147, 10.5194/acp-21-2125-2021, 2021.

956 Woodward-Massey, R., Sommariva, R., Whalley, L. K., Cryer, D. R., Ingham, T., Bloss, W. J., Ball, S. M.,  
957 Cox, S., Lee, J. D., Reed, C. P., Crilley, L. R., Kramer, L. J., Bandy, B. J., Forster, G. L., Reeves, C. E.,  
958 Monks, P. S., and Heard, D. E.: Radical chemistry and ozone production at a UK coastal receptor site,  
959 *Atmos Chem Phys*, 23, 14393-14424, 10.5194/acp-23-14393-2023, 2023.

960 Yang, X., Li, Y., Ma, X., Tan, Z., Lu, K., and Zhang, Y.: Unclassical Radical Generation Mechanisms in the  
961 Troposphere: A Review, *Environ Sci Technol*, 10.1021/acs.est.4c00742, 2024a.

962 Yang, X., Lu, K., Ma, X., Gao, Y., Tan, Z., Wang, H., Chen, X., Li, X., Huang, X., He, L., Tang, M., Zhu,  
963 B., Chen, S., Dong, H., Zeng, L., and Zhang, Y.: Radical chemistry in the Pearl River Delta: observations  
964 and modeling of OH and HO<sub>2</sub> radicals in Shenzhen in 2018, *Atmos Chem Phys*, 22, 12525-12542,  
965 10.5194/acp-22-12525-2022, 2022.

966 Yang, X., Wang, H., Lu, K., Ma, X., Tan, Z., Long, B., Chen, X., Li, C., Zhai, T., Li, Y., Qu, K., Xia, Y.,  
967 Zhang, Y., Li, X., Chen, S., Dong, H., Zeng, L., and Zhang, Y.: Reactive aldehyde chemistry explains the  
968 missing source of hydroxyl radicals, *Nat Commun*, 15, 1648, 10.1038/s41467-024-45885-w, 2024b.

969 Yang, X., Lu, K., Ma, X., Liu, Y., Wang, H., Hu, R., Li, X., Lou, S., Chen, S., Dong, H., Wang, F., Wang, Y.,  
970 Zhang, G., Li, S., Yang, S., Yang, Y., Kuang, C., Tan, Z., Chen, X., Qiu, P., Zeng, L., Xie, P., and Zhang, Y.:  
971 Observations and modeling of OH and HO<sub>2</sub> radicals in Chengdu, China in summer 2019, *The Science of  
972 the total environment*, 772, 144829-144829, 10.1016/j.scitotenv.2020.144829, 2021a.

973 Yang, Y., Li, X., Zu, K., Lian, C., Chen, S., Dong, H., Feng, M., Liu, H., Liu, J., Lu, K., Lu, S., Ma, X.,  
974 Song, D., Wang, W., Yang, S., Yang, X., Yu, X., Zhu, Y., Zeng, L., Tan, Q., and Zhang, Y.: Elucidating the  
975 effect of HONO on O<sub>3</sub> pollution by a case study in southwest China, *Sci Total Environ*, 756, 144127,  
976 10.1016/j.scitotenv.2020.144127, 2021b.

977 Yugo Kanaya, Renqiu Cao, Hajime Akimoto, Masato Fukuda, Yuichi Komazaki, Yoko Yokouchi, Makoto  
978 Koike, Hiroshi Tanimoto, Nobuyuki Takegawa, and Kondo, a. Y.: Urban photochemistry in central Tokyo:  
979 1. Observed and modeled OH and HO<sub>2</sub> radical concentrations during the winter and summer of 2004, *J  
980 Geophys Res-Atmos*, 112, 20, 10.1029/2007JD008670, 2007.

981 Yugo Kanaya, R. C., Shungo Kato, Yuko Miyakawa, Yoshizumi Kajii, Hiroshi and Tanimoto, Y. Y.,  
982 Michihiro Mochida, Kimitaka Kawamura, Hajime Akimoto: Chemistry of OH and HO<sub>2</sub> radicals observed

983 at Rishiri Island, Japan, in September 2003: Missing daytime sink of HO<sub>2</sub> and positive nighttime  
984 correlations with monoterpene, *J Geophys Res-Atmos*, 112, 10.1029/2006id007987, 2007.  
985 Zhang, G., Hu, R., Xie, P., Lou, S., Wang, F., Wang, Y., Qin, M., Li, X., Liu, X., Wang, Y., and Liu, W.:  
986 Observation and simulation of HO<sub>x</sub> radicals in an urban area in Shanghai, China, *Sci Total Environ*, 810,  
987 152275, 10.1016/j.scitotenv.2021.152275, 2022a.  
988 Zhang, G., Hu, R., Xie, P., Lu, K., Lou, S., Liu, X., Li, X., Wang, F., Wang, Y., Yang, X., Cai, H., Wang, Y.,  
989 and Liu, W.: Intercomparison of OH radical measurement in a complex atmosphere in Chengdu, China, *Sci  
990 Total Environ*, 155924, 10.1016/j.scitotenv.2022.155924, 2022b.  
991